aerospace

MDPI

Article

High Aspect Ratio Composite Wings: Geometrically Nonlinear Aeroelasticity, Multi-Disciplinary Design Optimization, Manufacturing, and Experimental Testing

Touraj Farsadi [1,2,*], Majid Ahmadi [1], Melin Sahin [3], Hamed Haddad Khodaparast [2], Altan Kayran [3] and Michael I. Friswell [2]

[1] Aerospace Engineering Department, Adana Alparslan Turkes Science and Technology University, Adana 01250, Türkiye; matehrani@atu.edu.tr
[2] Faculty of Science and Engineering, Swansea University, Swansea SA1 8EN, UK; h.haddadkhodaparast@swansea.ac.uk (H.H.K.); m.i.friswell@swansea.ac.uk (M.I.F.)
[3] Department of Aerospace Engineering, Middle East Technical University, Ankara 06800, Türkiye; msahin@metu.edu.tr (M.S.); akayran@metu.edu.tr (A.K.)
* Correspondence: tfarsadi@atu.edu.tr

Abstract: In the field of aerospace engineering, the design and manufacturing of high aspect ratio composite wings has become a focal point of innovation and efficiency. These long, slender wings, constructed with advanced materials such as carbon fiber and employing efficient manufacturing methods such as vacuum bagging, hold the promise of significantly lighter aircraft, reduced fuel consumption, and enhanced overall performance. However, to fully realize these benefits, it is imperative to address a multitude of structural and aeroelastic constraints. This research presents a novel aeroelastically tailored Multi-objective, Multi-disciplinary Design Optimization (MMDO) approach that seamlessly integrates numerical optimization techniques to minimize weight and ensure structural integrity. The optimized wing configuration is then manufactured, and a Ground Vibration Test (GVT) and static deflection analysis using the Digital Image Correlation (DIC) system are used to validate and correlate with the numerical model. Within the fully automated in-house Nonlinear Aeroelastic Simulation Software (NAS^2) package (version v1.0), the integration of analytical tools offers a robust numerical approach for enhancing aeroelastic and structural performance in the design of composite wings. Nonlinear aeroelastic analyses and tailoring are included, and a population-based stochastic optimization is used to determine the optimum design within NAS^2. These analytical tools contribute to a comprehensive and efficient methodology for designing composite wings with improved aeroelastic and structural characteristics. This comprehensive methodology aims to produce composite wings that not only meet rigorous safety and performance standards but also drive cost-efficiency in the aerospace industry. Through this multidisciplinary approach, the authors seek to underscore the pivotal role of tailoring aeroelastic solutions in the advanced design and manufacturing of high aspect ratio composite wings, thereby contributing to the continued evolution of aerospace technology.

Keywords: high aspect ratio wing; composite material; aeroelastic tailoring; multi-disciplinary design optimization; geometrical nonlinearity; numerical simulation

Citation: Farsadi, T.; Ahmadi, M.; Sahin, M.; Haddad Khodaparast, H.; Kayran, A.; Friswell, M.I. High Aspect Ratio Composite Wings: Geometrically Nonlinear Aeroelasticity, Multi-Disciplinary Design Optimization, Manufacturing, and Experimental Testing. *Aerospace* **2024**, *11*, 193. https://doi.org/10.3390/aerospace11030193

Academic Editor: Haichao An

Received: 24 January 2024
Revised: 21 February 2024
Accepted: 26 February 2024
Published: 28 February 2024

1. Introduction

Weight optimization directly influences the structural integrity of the aircraft and its aeroelastic performance. A lighter wing reduces stress in the structure, improves fuel efficiency, and enhances overall performance. It is vital for striking the right balance among structural, aeroelastic, and material requirements in high aspect ratiohigh aspect ratio wing designs [1]. These wings endure substantial bending and torsional loads,

demanding proper design to prevent failure. Thus, weight optimization should go hand in hand with structural analysis to ensure strength while maintaining lightness. Considerable research efforts have been devoted to the utilization of composite materials for the aeroelastic tailoring of aircraft wings, to minimize the structural weight. In numerous studies [2–8], the sizing of the structure is predominantly based on static maneuver load cases, incorporating design constraints such as stiffness, buckling resistance, static strength, control reversal, and both static and dynamic aeroelastic stability. Dynamic aeroelasticity [9–12] is indispensable in wing optimization as it unveils critical aspects not apparent in static aeroelasticity. It aids in identifying flutter, which is crucial for avoiding dangerous scenarios, and provides insights into time-dependent behaviors such as vibrations and resonances, addressing issues of passenger comfort and structural fatigue. This comprehensive understanding is essential for optimizing wing designs in terms of stability, safety, longevity, and gust response. These investigations emphasize the critical role of composite materials in achieving optimal structural performance under diverse loading conditions, ensuring not only structural integrity but also addressing aeroelastic considerations for enhanced overall aircraft efficiency and safety. Various types of fluid-structure interaction instabilities, including flutter, vortex-induced vibration, and vortex shedding, manifest in aerospace components, wings, and their control mechanisms. Several studies have reported on CFD-based simulations to elucidate these phenomena [13–15].

Mitrotta et al. [16] introduced an innovative design methodology using Proteus, OptiBLESS, and MSC Nastran for aeroelastic tailoring, optimization, and analysis, respectively. Employing the Multidisciplinary Design Optimization (MDO) approach across various studies [17–22], they focused on minimizing wing weight under both static and dynamic aeroelastic conditions. Benaouali and Kachel [23] automated the numerical simulation for optimizing aircraft wings, achieving an 8.9% range increase by considering design variables. Sinha et al. [24] showcased the strength-to-weight superiority of composite wings over aluminum using DLR-AE automated aeroelastic software (version v.3), cpacs-MONA. Silva et al. [25] optimized composite wings, considering strength, buckling, and flutter criteria. Saporito et al. [26] developed a framework for early-stage conceptual design, integrating dynamic aeroelastic constraints for aircraft wing optimization. Highlighting the importance of incorporating aerodynamic loads in the optimization of wing structure, Rajpal et al. [27] emphasized the need for a comprehensive approach. Kilimtzidis and Kostopoulos [28,29] proposed a numerical algorithm for obtaining the optimal stacking sequence of high aspect ratio composite wings, considering static aeroelasticity. However, there remains limited literature on experimental datasets for tailored composite wings. Early research has focused on the testing of wings modeled as plates [30,31], which are tailored to enhance the aeroelastic behavior through the bend-twist coupling of the composite laminate. A concentrated effort on optimization, manufacturing, and testing of an aeroelastically tailored wing with a representative cross-section using composite materials was made at the German Aerospace Center (DLR) [32–35]. In these studies, the wing is manufactured using load-carrying skins filled with foam, with the foam serving to provide resistance against buckling. Ribs and spars are intentionally omitted from the wing to simplify the manufacturing process. Meddaikar et al. [32] investigated aeroelastic tailoring in composite wing design for optimized stiffness. Wind tunnel tests confirm the design's validity, aligning well with simulations. The paper gives an overview of the optimization framework, wing manufacturing, and experimental setup, presents wind tunnel results compared to simulations, and concludes with key findings. The absence of ribs and spars led to the exclusion of buckling constraints in the optimization, as thick laminates would be necessary to address the large buckling field. Turgut [36] focuses on the manufacturing of a lightweight composite wing. The study aims to contribute insights into optimizing the design and performance of UAV wings through a holistic examination of manufacturing processes, material properties, and structural considerations. Validating a numerical design approach for optimizing composite wings under gust and fatigue loading, Rajpal et al. [37] demonstrated its effectiveness. In contrast to

traditional methods, they employed an analytical fatigue model to enhance accuracy and exploit the potential of composite materials. A critical rectangular composite wing is designed, manufactured, and tested in the wind tunnel, and fatigue experiments are performed to validate both aeroelastic and fatigue predictions. The study confirms the success of the design methodology yet highlights stiffness degradation due to fatigue, affecting the aeroelastic response.

For analyzing static and dynamic aeroelasticity in aircraft with highly flexible, high aspect ratio wings that experience significant in-flight deflections under operational loads, the geometrically linear approach proves inadequate. Structural and aerodynamic properties are altered by these deflections, impacting stability boundaries and introducing new instability mechanisms. Therefore, an essential requirement for accurate aeroelastic analysis is the utilization of a geometrically nonlinear approach [38–40]. A framework is proposed by Gray et al. [41] that integrates geometrically nonlinear, subsonic flutter constraints into aerostructural optimization. An effective framework using nonlinear Reduced Order Models (ROM) for flutter and gust responses is introduced by Chao et al. [42]. Ensuring accurate calculation of critical constraints for flutter-free designs necessitates a geometrically nonlinear analysis approach involving static equilibrium computation, linearization, eigenvalue determination, and flutter boundary calculation for optimizing highly flexible wings. The impact of follower load and geometrical nonlinearity on a highly flexible wing's aeroelastic dynamics is investigated by Riso and Cesnik [43,44], revealing that linear kinematics may overstate static deflections at high angles of attack (AOA) by up to 50%. The present work explores, for the first time, the incorporation of geometrical nonlinearity in the MDO analysis of a composite wing. The findings reveal significant differences when compared to traditional isotropic wing models.

The literature review identifies several gaps in current research on high aspect ratio wing design and optimization. Firstly, while considerable effort has been devoted to utilizing composite materials for aeroelastic tailoring of aircraft wings, there remains a lack of comprehensive studies addressing the simultaneous consideration of structural, aeroelastic, and material requirements in high aspect ratio wing designs. Existing studies primarily focus on static maneuver load cases for sizing the structure, overlooking dynamic aeroelasticity, which is critical for identifying flutter and understanding time-dependent behaviors such as vibrations and resonances.

Moreover, there is limited literature on experimental datasets for tailored composite wings, with early research primarily focusing on testing wings modeled as plates rather than representative cross-sections. While some studies have the explored optimization, manufacturing, and testing of aeroelastically tailored wings using composite materials, there is still a gap in comprehensive investigations that integrate all these aspects.

Additionally, current approaches to aeroelastic analysis often utilize geometrically linear methods, which may not accurately capture the behavior of highly flexible wings experiencing significant in-flight deflections. Incorporating geometric nonlinearity is crucial for accurately predicting stability boundaries and instability mechanisms in such wings, yet there is limited research on applying this approach in multidisciplinary optimization (MDO) analysis of composite wings.

Furthermore, this study offers benchmark numerical and experimental data for an optimized high aspect ratio composite wing, serving as a valuable reference point for comparison by other researchers. By addressing the practical challenges inherent in this multidisciplinary field, the findings of this research contribute to a deeper understanding of composite wing design and offer guiding implications for future endeavors in aerospace engineering.

Consequently, this paper's significance and innovations can be succinctly summarized as follows:

- The study proposes a novel MMDO method to optimize the performance of a composite UAV wing by addressing structural, material, aeroelastic, and manufacturing constraints. It focuses on key variables such as upper and lower skin region

dimensions and layup stacking sequence, spar thickness, and rib placement to address critical aspects such as buckling, deformations, stress limits, and composite failure.

- Examining the influence of large deformations on aeroelastic instability limits and failure mechanisms, this paper emphasizes the importance of addressing geometrically nonlinear constraints. The study makes a significant contribution to optimizing highly flexible composite wings by highlighting the need to consider geometric nonlinearity.
- The paper introduces NAS^2, a fully automated in-house software for optimizing and designing composite aircraft structures.
- Manufacturing, material characterization, and experimental tests are conducted on the optimized composite wing to validate the NAS^2 in-house software and to correlate the finite element numerical model. Also, the study aims to gain insights into the practical challenges of this multidisciplinary field. This research distinguishes itself from a limited number of studies concentrating on the experimental facets of high aspect ratio composite aircraft wing design, offering a unique level of comprehensiveness.

The process of multidisciplinary research necessitates a clear and succinct description at the outset, typically facilitated by a technical flowchart as shown in Figure 1. Integrating these components offers a clear and streamlined roadmap for the multidisciplinary research process involved in the design and manufacturing of aircraft wings.

Figure 1. Technical flowchart.

2. General MDO Framework

The primary aim of this research is to create an enhanced aeroelastic scenario for composite aircraft wings, aiming to boost performance while simultaneously reducing overall weight by applying a novel MDO. The approach involves the utilization of an integrated Nonlinear Aeroelastic Simulation Software (NAS^2) package tailored for aircrafts to develop composite wing models. Optimization primarily centers on strategically placing and orienting fibers in multiple distinct regions along the wing's span to improve structural integrity, aeroelastic performance, and minimize weight.

Employing the Particle Swarm Optimization (PSO) algorithm, this study pursues the optimization of variables related to the composite layer arrangement, order, fiber angle, and spanwise division areas of the wing. Encompassing considerations such as minimum safety factors, aeroelastic stability regarding flutter and divergence speeds, gust loading,

a fabricated method, and the prevention of primary and secondary (shear) buckling and composite failure, the PSO algorithm is designed to navigate within specified design constraints. The overarching goal of the optimization process is to minimize the wing weight while simultaneously maximizing the unit twist factor. Investigating the potential for torsion-bending coupling in the composite wing, this research determines the unit twist factor through the ratio of the twist to the vertical deflection at the wing tip.

Figure 2 visually delineates the procedure and results of the PSO algorithm, illustrating the design structure matrix (DSM) of the MDO at two levels. At optimizer level #1, structural and composite analysis is conducted, and the convergence of the inner loop precedes the execution of level #2 (outer loop), which focuses on the aeroelastic aspect. At optimizer level #2, gust analysis, aeroelastics, and structural dynamics are incorporated. The optimization matrix undergoes an initial linear execution in the inner loop to establish approximate parameter limits, followed by a non-linear execution in the second step. This entire process showcases the outcomes achieved through the PSO algorithm.

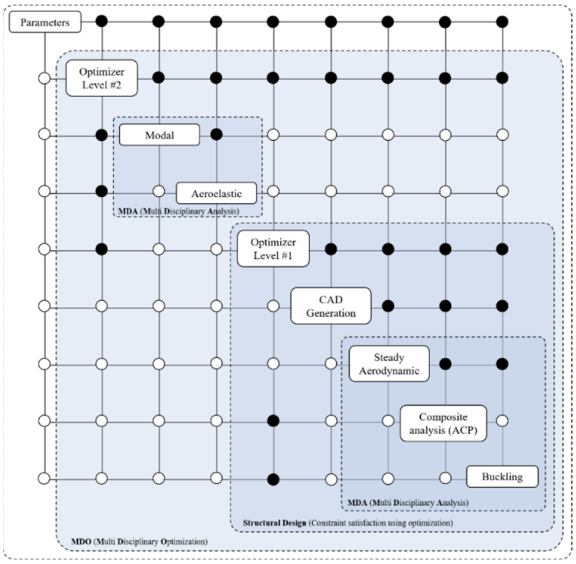

Figure 2. Design structure matrix (DSM) of the MDO.

The black nodes in the Design structure matrix (DSM) of the Multi-Disciplinary Optimization (MDO) diagram represent critical coupling points or interfaces between different components or disciplines within the optimization process. These nodes indicate areas where significant interactions or dependencies exist, requiring careful consideration and analysis during the optimization process. On the other hand, the white nodes represent components or disciplines that are relatively independent or have fewer interactions with other parts of the system. These nodes may still play essential roles in the overall optimization process but may not require as much attention or analysis as the critical coupling points represented by the black nodes. The differentiation between black and white nodes helps to visually highlight the critical areas of the optimization process where closer examination and careful management of dependencies are necessary for successful optimization outcomes.

Presenting an overview of the MDO problem, Table 1 aims to craft a lightweight and highly flexible wing by simultaneously minimizing the overall weight and maximizing the unit twist factor. Several laminates are formed by dividing the upper and lower skins into spanwise regions. The optimization process focuses on particular laminates within both the upper and lower skins, in addition to addressing the spar and the ribs. The optimization endeavor involves minimizing the combined function f($\mathbf{x}$), representing the trade-off between the wing weight reduction and the unit twist factor maximization. The

design variables (**x**) encompass parameters such as the lengths of regions for the top and lower skins, the number of layers for each skin, fiber angles, and rib positions. Constraints related to buckling, static strength, composite failure, and aeroelastic instability shape the optimization problem, which further considers three load cases: static, dynamic, and gust loads.

The optimization aims to produce results that are not only optimal in terms of structural and aeroelastic constraints but also feasible and manufacturable. This involves imposing limitations on the used discrete ply angles, with increments of 5 degrees, and section length, with a step size of 1 cm. These constraints are introduced to ensure that the optimized design can be practically realized in the manufacturing process.

The other issue is that the relationship between ply angle and section length introduces a constraint that limits the maximum achievable ply angle as the section length increases (See Figure 3). This constraint is expressed through a specific equation, and its inclusion is crucial to reflect the practical consideration of maintaining each layer as a single, continuous piece. As the section length grows, this constraint helps in determining the appropriate ply angle to maintain manufacturability while optimizing other design parameters.

Table 1. Optimization problem.

Objectives: Minimize the combined objective function f(**x**) representing the trade-off between minimizing the wing weight and maximizing the unit twist factor:

f(**x**) = Wing Weight(**x**) − λ × Unit Twist Factor(**x**)

where **x** is the vector of design variables, and λ is a weight factor.

Variables: Design variables (**x**):

Length of regions for the upper skin, L_i^U

Length of regions for the lower skin, L_i^L

Number of layers for the upper skin, N_i^U

Number of layers for the lower skin, N_i^L

Number of layers for the spar, N^S

Fiber angle for the upper skin, θ^U

Fiber angle for the lower skin, θ^L

Fiber angle for the spar, θ^S

Rib positions, pos^R

Constraints: The optimization problem is subject to the following constraints:

*Load Multiplier: Buckling(***x***),*

*Inverse Reverse Factor: Static Strength(***x***)* and *Composite Failure(***x***)*

*Flutter and Divergence: Aeroelastic Instability(***x***)*

Manufacturability: See Figure 3

$$\theta_{max} = tan^{-1}\left(\frac{-L^2 b - c\sqrt{L^2(L^2 - b^2 + c^2)}}{\left(-bc + L\sqrt{L^2(L^2 - b^2 + c^2)}\right)}\right)$$

Load Cases: The optimization considers three load cases:

Static Load (Function of *flight speed (V)* and *AOA (α)*)

Dynamic Load (Function of *flight speed (V)* and *AOA (α)*)

Gust Load (Function of *gust frequencies* (F) and *gust velocities* (WG))

Exploring sensitivity, Pareto analysis, and robustness considerations is essential within the framework of Multidisciplinary Design Optimization (MDO). This comprehensive approach involves evaluating how variations in parameters impact the overall design, navigating the trade-offs presented in Pareto fronts, and ensuring the design's resilience to uncertainties through robustness analysis. Integrating these aspects in MDO enhances the holistic understanding and optimization of complex systems, leading to more informed and reliable engineering solutions.

Figure 3. Ply angle and section length, where, the fiber fabric width is *b*, the ply lamina width is *c* and each lamina's length is *L*.

3. Geometrical Nonlinear Analysis

A comprehensive analysis is indispensable to enhance the performance of a high aspect ratio composite wing. This analysis should cover the examination of composite and structural failures, aeroelastic instabilities (flutter and gust analysis), buckling analysis, and the consideration of geometric nonlinearities. Overlooking any of these factors may result in suboptimal outcomes. This investigation underscores the importance of incorporating geometric nonlinearity for achieving optimal performance in composite wings. Initial numerical analysis has revealed that substantial static deflections in wings with high aspect ratios lead to alterations in structural natural frequencies, affecting flutter onset points and mechanisms. Geometrically nonlinear analysis is imperative to precisely address significant deformations and rotations, which are essential for optimizing the wing's design.

This study introduces a novel approach to accounting for geometrical nonlinearity in calculations. While previous research has explored this method in simple and isotropic wings such as the Pazy wing, our investigation reveals that composite wings with intricate configurations and stacking sequences exhibit distinct behavior compared to isotropic wings when employing geometrical nonlinear techniques in calculations. The assertion that linear kinematics exaggerates the aeroelastic static deflection of high aspect ratio wings compared to geometrically nonlinear kinematics may lack accuracy for composite wings. This discrepancy arises when accounting for follower force and the effects of geometrical nonlinearity in the aeroelastic governing equation. In certain instances, linear kinematics may, in fact, underestimate the static deflection, and the real deformation can surpass what the linear formulation suggests.

This study places particular emphasis on incorporating geometrical nonlinearity into the MDO framework for both static and aeroelastic calculations. In the optimization of the wing design through a geometrically nonlinear analysis approach, the following four stages are essential: *Nonlinear Static Equilibrium Computation:* Compute the static equilibrium of a nonlinear aeroelastic system of the aircraft at various flight conditions by solving the nonlinear aeroelastic set of dynamic equations for the wing. This step is crucial for understanding the static configuration of the wing during flight. *Equilibrium State Linearization:* Approximate the nonlinear equations by linearizing them around each equilibrium state through coupled linear equations. This allows the description of the system's behavior in proximity to the equilibrium state. *Aeroelastic Eigenvalue Determination:* The eigenvalues of the locally linearized systems are calculated by employing the linearized equations of motion. Information about the natural frequencies and damping ratios of the wing is provided by these eigenvalues, offering insights into its stability and dynamic response

during flight. *Standard Eigenvalue Analysis:* Conduct an analysis of aeroelastic eigenvalues on the state space form of governing equations to obtain eigenvectors and eigenvalues. These results are then used to evaluate constraints or can be post-processed for further analysis purposes, contributing to the comprehensive optimization of the wing design.

4. Nonlinear Aeroelastic Simulation Software (NAS²)

Developed in the Advanced Simulation Laboratory at Adana Science and Technology university, the optimization process is automated through the in-house Nonlinear Aeroelastic Simulation Software (NAS²). Tailored for the analysis of aeroelasticity and structural aspects of aircraft components, NAS² aims to offer precise and consistent results while reducing computational time and costs. It facilitates several analyses, including static analysis, free vibration analysis, aeroelastic and gust analysis, as well as composite analysis and optimization.

NAS² comprises several distinct modules, namely the *Model module* (encompassing an in-house Graphical User Interface (GUI) and models imported from CAD softwares 2020), the *Aerodynamic Analysis module*, the *Structural and Composite Analysis module*, the *Reduced Order Aeroelastic Analysis module*, and the *Optimization module*. Here are the features of NAS²:

- NAS² relies on a combination of in-house-developed codes, open-source tools, and commercial software, selected based on availability and the required fidelity for specific projects. The interface is crafted using C# (C-Sharp), while the core code is written in C++ and FORTRAN. The automatic creation of the structured grid without user interference via intelligent algorithms is facilitated in the model module.
- The structural model within NAS² encompasses both linear and nonlinear structural beam and shell models that can be seamlessly imported from open-source and commercial software. Additionally, it incorporates specialized in-house models such as the Geometrically Exact Beam Theory (GEBT) [45], the nonlinear shell model [21], and the geometrically nonlinear Thin Wall Beam (TWB) model [38,39]. Cross-sectional properties are computed using VABS (Variational Asymptotic Beam Sectional Analysis) [46] and in-house software based on the Librescu thin wall beam theory [47–49], accounting for nonlinear and coupling stiffness terms. Both the first and secondary warping models are considered in the theory. The structural solver employs the finite element (FE) method. The structural model incorporates viscoelastic models to represent structural damping [50].
- The integration of ANSYS ACP with NAS² forms a powerful alliance, particularly in the realm of composite failure analysis. ANSYS ACP, renowned for its expertise in handling composite materials, complements the computational capabilities of NAS².
- For aerodynamic modeling, NAS² employs the Vortex Lattice Method, in-house 3D panel theory [51], strip theory (incompressible and compressible aerodynamics) [39], and piston theory [52]. Aerodynamic loads can be imported from MSC NASTRAN [53] and ZONA ZAERO [54] commercial software. To expedite the solution of nonlinear aeroelastic problems, an in-house nonlinear ROM has been developed.
- NAS² adopts a range of discrete gust models [55,56] for application in studies focused on gust load alleviation, particularly tailored for high-aspect ratio wings. These wings exhibit heightened susceptibility to fracture when exposed to gusts.
- The coupling algorithm within NAS² orchestrates the seamless interaction of all the aforementioned modules, enabling the attainment of fully nonlinear simulations. This comprehensive approach ensures that NAS² is well-equipped to handle diverse engineering projects, offering a sophisticated and integrated solution for structural and aerodynamic analyses, particularly in the context of aeroelastic optimization of high aspect ratio composite wings.

- The NAS² package integrates two optimization algorithms, namely Genetic Algorithm (GA) [57] and Particle Swarm Optimization (PSO) [58], with other modules to execute a Multidisciplinary Design Optimization (MDO) procedure seamlessly.

5. Design Framework

5.1. Structural Analysis

The prediction of buckling onset begins with linear buckling analysis, suitable for small deformations but less effective for high aspect ratio wings undergoing substantial deformations. Nonlinear buckling analysis, accounting for geometric nonlinearities, becomes crucial to accurately capturing large deformations. Influenced by stress direction and wing geometry, including primary Euler buckling and secondary modes such as shear or web buckling, this approach offers a prediction of the structural performance, revealing buckling manifestations in various modes. To comprehensively analyze the composite wing structure, finite element analysis (FEA) is employed, integrating primary and secondary buckling equations considering structural intricacies, material properties, and loading conditions. FEA, through numerical simulations, calculates critical loads and buckling modes, providing a detailed understanding of the wing's structural behavior.

On the other hand, the assessment of the composite wing's strength involves applying the Tsai-Wu failure principle [59], deriving the in-plane stress state through elastic FEA, and determining strength ratios using in-plane stress components. Investigating out-of-plane failure additionally involves capturing delamination occurrences with a quadratic stress criterion [11,59] and establishing surface-based cohesive behavior between adjacent layers.

Inverse Reverse Factor (IRF)

The IRF, in the context of safety analysis, serves as a complementary metric to the Safety Factor (SF). While the Safety Factor quantifies the margin of failure by multiplying the applied load, the IRF provides an inverse perspective by representing the failure load as the applied load divided by the IRF. A Safety Factor greater than one signifies a positive margin to failure, whereas an inverse reverse factor greater than one indicates a potential for failure. The formula for IRF is defined as the reciprocal of the Safety Factor (IRF = 1/SF). Critical values of reserve factors fall within the range of zero to one, while non-critical values span from one to infinity. Parameters such as fiber failure, matrix failure, in-plane shear failure, out-of-plane shear failure, delamination, and the Tsai-Wu factor are considered, contributing to a comprehensive evaluation of the composite structure's safety margins (SM = SF − 1). The emphasis on non-critical values, whether presented numerically or through contour plots, highlights their significance in comparison to critical values.

5.2. ROM Aeroelastic Analysis (Flutter and Gust Analysis)

The flowchart presented in Figure 4 provides a comprehensive illustration of the flutter solution and the optimization procedure. Within the optimization flowchart, two primary loops are distinguished: one inner loop, which is designed to satisfy the static structure constraints using optimization, called "Constraint satisfaction using optimization" and an outer loop, which checks the dynamic structural constraints (aeroelastic stability). Following the extraction of the wing's geometrical configuration from the optimization process, a nonlinear static aeroelastic analysis is executed to calculate significant static deflections, capturing the static equilibrium point upon convergence of the iterative process. For each deformed shape, updated aerodynamic loads based on the deformed structure shape are calculated until convergence is achieved. A post-convergence check is conducted for buckling and static constraints to ensure compliance with optimization constraints. If there is an unsatisfied constraint, the optimizer updates the inputs' bounds and repeats the loop until all constraints are satisfied. Subsequently, flutter analysis is performed around the static equilibrium point obtained from the nonlinear static aeroelastic

analysis, utilizing a reduced-order model. Modal analysis is executed to acquire mode shapes and natural frequencies, and the first few modes are incorporated into the reduced-order model for flutter analysis until convergence is reached. The P-k method is then applied to construct aeroelastic frequency and damping diagrams, providing insights into the flutter speed, frequency, and modes contributing to instability. At this point, if the instability speed is within the accepted range, the optimization loop ends.

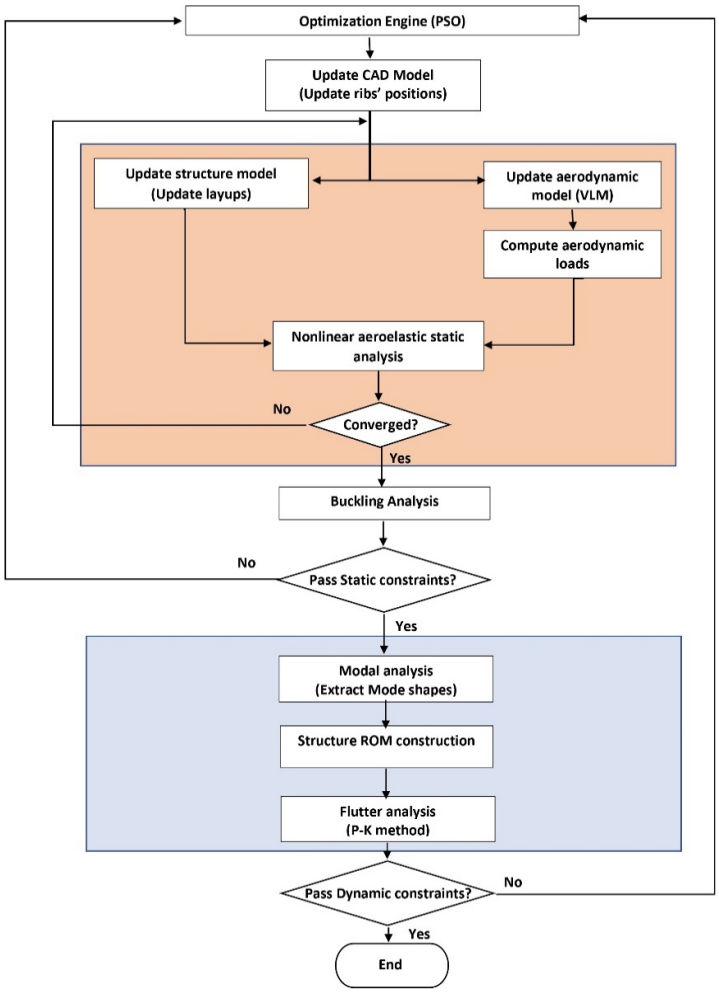

Figure 4. Aeroelastic solution and optimization procedure.

In the present work, gust response and Flutter analyses were conducted using the Vortex Lattice Method (VLM). To introduce discrete gust velocity into the VLM-based aerodynamic model, the freestream velocity can be modified, and the vortex lattice can be updated. In the current investigation, a 1-cosine gust model [55,60] is applied, as shown in Equation (1), where the maximum magnitude of the vertical gust speed is denoted by V_{ds}. V_g(t) represent the gust velocity as a function of time t. The ratio between V_{ds} and V is represented by WG, with gust frequency denoted by F, and time by t. It is supposed that the gust shape has a length of $2H$. Thus,

$$\frac{V_g}{V} = \begin{cases} \frac{WG}{2}[1 - \cos(2\pi F t)], & t < T \\ 0, & t \geq T \end{cases} \quad (1)$$

where,

$$F = \frac{1}{T}, T = \frac{2H}{V}, WG = \frac{V_{ds}}{V}$$

6. Numerical Results and Discussions

6.1. Numerical Validation of NAS²

Figure 5 presents a visual comparison between the distributed pressure obtained through NAS²'s 3D panel solver and a parallel Computational Fluid Dynamics (CFD) simulation using FLUENT as a static aeroelasticity validation. The wing model has a length of 12.15 m, with a chord length ranging from 120 cm at the root to 60 cm at the tip. Calculations are conducted at a speed of 100 km/h under sea-level atmospheric conditions with an AOA (α) set at 10°. Concurrently, Table 2 details the findings of the flutter analysis performed on the Goland wing [61,62], employing NAS²'s VLM solver as the linear dynamic aeroelasticity validation.

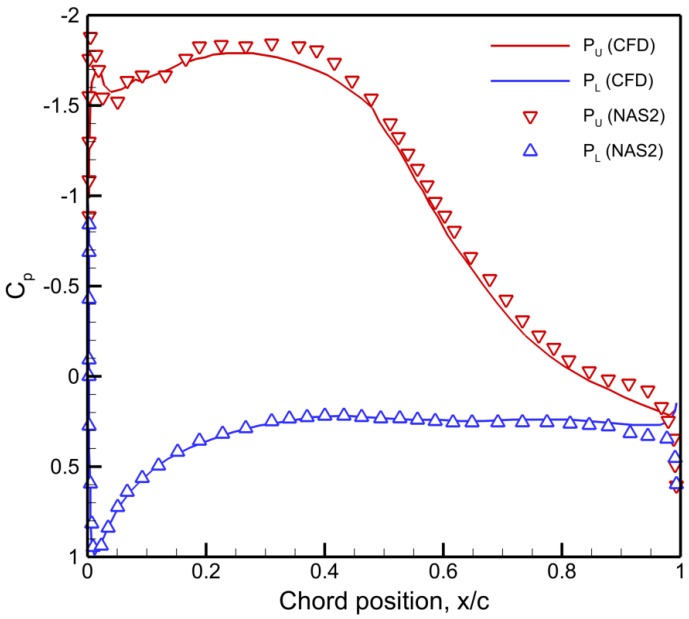

Figure 5. Comparing the wing's pressure distribution obtained from NAS² with the results from CFD.

In order to verify the accuracy of the incorporated aeroelastic model, the instability speed of a Goland wing has been computed. The wing under consideration has a span of 6.09 m, a chord of 1.83 m, and an elastic axis positioned at 33% from the leading edge. Torsional and bending stiffness values are assigned as 987.1 KNm² and 9.77 MNm², respectively. Table 2 compares the results obtained from NAS² with those documented in references [61,62] for the Goland wing.

Table 2. The flutter speed and frequency of Goland's wing.

	Instability Speed (m/s)	Instability Freq. (rad/s)
NAS²	164	64
Murua et al. [61]	165	69
Wang et al. [62]	164	-

In validating nonlinear aeroelastic calculations in NAS², the study by Riso and Cesnik [43] is a key reference exploring geometrically nonlinear effects in the aeroelastic dynamics of the flexible Pazy wing. A detailed comparative analysis, contrasting NAS² results

with those in ref. [43], is presented in Table 3. Input data for this rigorous analysis is meticulously sourced from their dedicated GitHub repository [43]. Examining flow velocities of 30, 40, 50, and 60 m/s with a fixed root AOA at 5 degrees, observations reveal modest deformations at 30 m/s and increasing nonlinearly at 50 and 60 m/s.

Table 3. Selected non-dimensional vertical tip deflection at $\alpha = 5°$.

V (m/s)	30	40	50	60
NAS[2]	10	18.59	30.29	43.98
Fully nonlinear [43]	9.87 (−1.3%)	18.57 (−0.11%)	30.41 (0.4%)	44.28 (0.68%)
Non-follower loads [43]	9.82 (−1.8%)	18.22 (−1.99%)	28.94 (−4.46%)	40.39 (−8.16%)
Linear kinematics [43]	9.98 (−0.2%)	19.32 (3.93%)	34 (12.25%)	57.72 (31.24%)
Fully linear [43]	9.98 (−0.2%)	19.31 (3.87%)	34 (12.25%)	57.71 (31.22%)

6.2. Case Study—Wing Model

As an example, a composite UAV wing is optimized using the proposed approach. The composite wing features a half span of 1.25 m, showcasing a sleek design with a sweep angle of 0 degrees. The spar is strategically located at a 25% chord, contributing to the overall structural integrity. With a high aspect ratio of 14 and a taper ratio of 1, the wing exhibits a well-balanced geometry. The airfoil employed for this composite wing is the NACA 0010, chosen for its aerodynamic properties. This combination of design elements and specifications aims to optimize the overall performance and functionality of the composite wing shown in Figure 6 in diverse aeroelastic and structural scenarios. While showcased in this specific example, the flexibility and comprehensiveness of the framework are demonstrated. Specifically, the approach can be tailored for any new configuration by adjusting input parameters, highlighting its adaptability. In Figure 6, the lengths along the span in the upper skin are denoted as L_1^U, L_2^U and L_3^U, while in the lower skin, they are represented as L_1^L, L_2^L and L_3^L.

In this study, a circular tube spar is manufactured and used in the composite wing. The efficiency of a circular tube spar in a UAV high aspect ratio wing is a multifaceted consideration, encompassing factors such as weight-to-strength ratio, stiffness, manufacturing simplicity, cost-effectiveness, aerodynamic performance, structural integration, fatigue resistance, safety, and redundancy. Their straightforward manufacturing and cost-effectiveness further contribute to overall efficiency, with a focus on seamless integration into the wing structure. The optimization procedure includes partitioning the wing into three separate regions, encompassing both upper and lower skins, the spar, and the ribs. Furthermore, independent optimization is applied to the upper and lower skins within each region. Significantly, there is a gradual reduction in the overall thickness and the number of composite layers from the root to the tip, corresponding to the changing bending moments experienced across the wing's span. This reduction in layer thickness, known as ply drop, occurs when transitioning between different wing sections, resulting in a thinner composite laminate at that specific location. The study also considers the presence of nine ribs with varying distances along the wing's span.

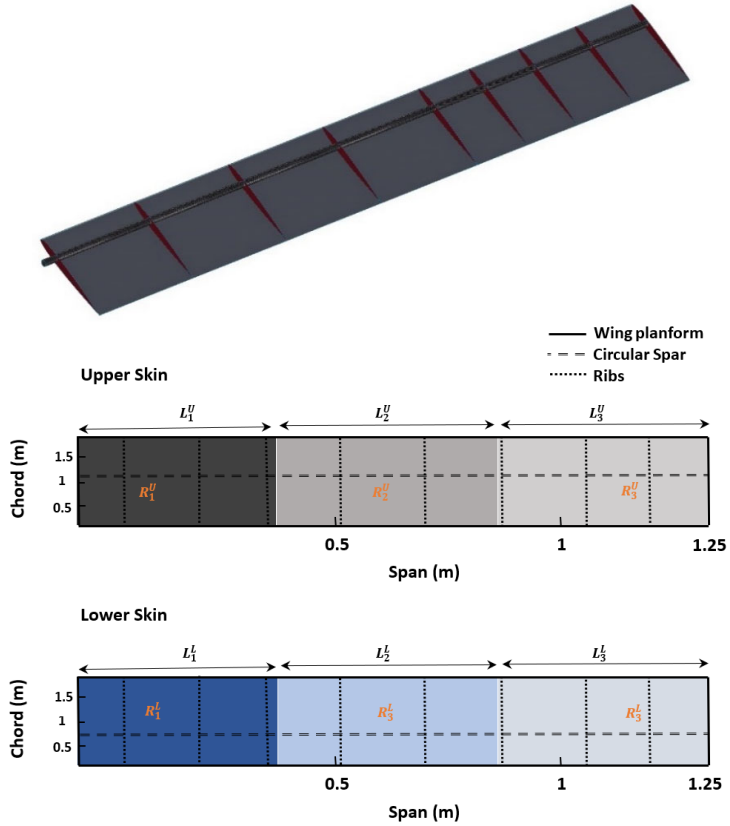

Figure 6. Graphical representation of baseline wing configuration as a case study. The design regions are indicated by different colors in the upper and lower skins.

By forming a total of seven distinct laminates by dividing the upper and lower skins into three spanwise laminates and the spar into a single laminate, flexibility is provided in terms of being either unbalanced or symmetric. The optimization procedure meticulously targets specific laminates within the upper and lower skins, as well as the spar, while assigning predetermined laminates to the ribs. The primary objective is to design the wing in accordance with the specified optimization parameters (objectives, variables, constraints, and load cases) and boundaries detailed in Table 4.

Table 4. Optimization parameters and boundaries.

Objectives: f(**x**) = Wing Weight(**x**) − λ × Unit Twist Factor(**x**)
Variables: L_i^U *[mm] (0 to 1250);* L_i^L *[mm] (0 to 1250);* N_i^U *(2 to 16);* N_i^L *(2 to 16);* N^S *(fixed at 4);* θ^U *[°](−90 to 90);* θ^L *[°](−90 to 90);* θ^S *[°](−90 to 90);* pos^R *[mm] (0 to 625)*
Constraints: *Buckling*(**x**) ≥ *1.1; Static Strength*(**x**) ≤ *0.9; Composite Failure*(**x**) ≤ *0.9; Aeroelastic Instability*(**x**) ≥ *75 m/s*
Load Cases: *Static Load and Dynamic Load (V = 30 m/s,* α *= 5° &* α *= −2.5°)* *Gust Load (F (1 to 20);* WG *(0.1 to 1))*

In the present case study, in the Structural and Composite Analysis module of the NAS² package tool, static aeroelastic analysis utilizes the 3D panel method for structural analysis. Composite failure analysis, involving the calculation of the inverse reverse factor, is performed using embedded ANSYS ACP inside the Structural and Composite Analysis module of the NAS² package tool. In the Reduced Order Aeroelastic Analysis module,

the gust response analysis and flutter analysis are conducted using the VLM method. In the Optimization module, the minimization of weight, considering aeroelastic structural and composite constraints, is achieved through the application of the PSO optimization strategy.

The study encompasses the manufacturing of the optimized wing using carbon fibers, employing hand layup and vacuum bagging techniques. Subsequent experimental tests, including the Ground Vibration Test (GVT) and static deflection analysis using the Digital Image Correlation (DIC) system, are conducted to validate simulation outcomes, fine-tune parameters, and ensure adherence to safety standards. These experimental tests are crucial for identifying any disparities between simulations and real-world data, guiding necessary model refinements, and driving improvements in engineering and design. Beginning with an initial structural wing design, the process progresses to subsequent structural composite and aeroelastic analyses. Integrated into an optimization algorithm, these findings transform the wing design into a multidisciplinary engineering challenge. The optimization addresses practical limitations, ensures structural integrity, and verifies the viability of the solution across different aspects. An objective function, considering various metrics and constraints, establishes a quantifiable measure of the wing's structural and aeroelastic performance.

6.2.1. Stacking Sequence of the Optimized Composite Wing

Pursuing the selection of the optimum wing model that adheres to the principles of minimizing wing weight, maximizing the unit twist factor, and mitigating the critical failure parameter (characterized as the inverse reverse factor), the indispensable mathematical construct known as the Fitness Factor comes into play as shown in Equation (2).

To enhance scientific rigor, the parameters undergo non-dimensionalization, scaling them to a standardized range from 0 to 1. The process is designed so that the optimal value for each objective and parameter (min. wing weight, max. unit twist factor, and min. inverse reverse factor) is set to 1, while the remaining values are assigned numerical values between 0 and 1 in relation to the optimal value of 1.

$$\frac{(C_1 \times \text{wing weight}) + (C_2 \times \text{unit twist factor}) + (C_3 \times \text{inverse reverse factor})}{C_1 + C_2 + C_3} = \text{Fitness factor} \quad (2)$$

In this methodology, weight coefficients ($C_i, i = 1,2,3$) are assigned to each objective, defining their relative significance in the design process. The Fitness Factor, applied in the current study, utilizes a weighting system attributing $C_1 = 6, C_2 = 2$ and $C_3 = 1$ to wing weight, unit twist factor, and inverse reverse factor, respectively. Assigning the highest weight coefficient to wing weight underscores its paramount importance in optimization. The Fitness Factor quantifies the overall performance of each case study by effectively balancing objectives and their weight coefficients. Optimal design point selection, guided by the highest Fitness Factor, aligns with overarching design objectives while addressing critical failure parameters, particularly the inverse reverse factor. The Fitness Factor is computed for several case studies, ensuring the final wing design aligns with goals and adheres to robust mathematical and engineering principles. The first design point, demonstrating effectiveness with a Fitness Factor of 0.83, is noteworthy (see Figure 7). Comparative analysis reveals the second design's higher inverse reverse factor, albeit with a lower unit twist factor and reduced weight. Given the study's multi-objective nature, a thorough examination of all primary design points is imperative, considering their respective Fitness factors.

Utilizing bending-torsion coupling is a common strategy for managing loads in composite wing structures. This study investigates the influence of fiber layout on bending-torsion coupling, using the unit twist factor as an optimization objective. Decreasing fiber angles along the spanwise axis increases flapwise displacement, while increasing angles enhances bending-torsion coupling. A zero-degree fiber angle is assigned to the fibers oriented toward the wing tip in the spanwise direction. The unit twist factor is a key metric

for assessing this coupling in composites, irrespective of the wing bending stiffness. Importantly, employing off-axis fiber angles induces bending-torsion coupling in composite wings, thereby reducing loads.

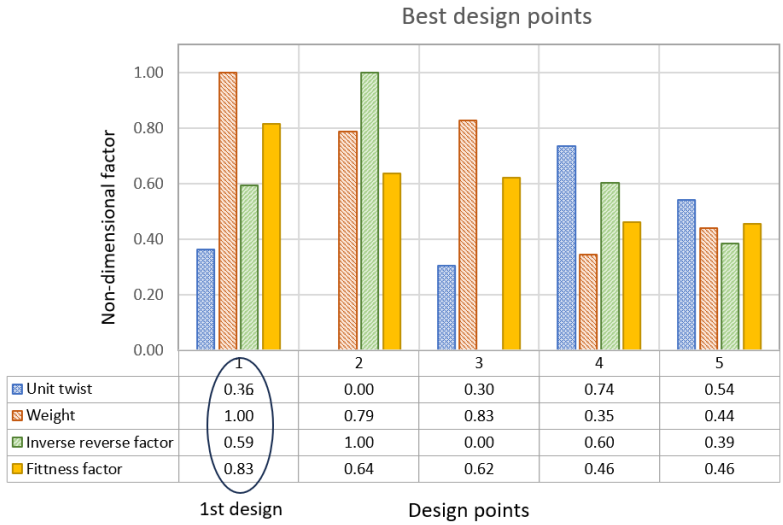

	1	2	3	4	5
Unit twist	0.36	0.00	0.30	0.74	0.54
Weight	1.00	0.79	0.83	0.35	0.44
Inverse reverse factor	0.59	1.00	0.00	0.60	0.39
Fittness factor	0.83	0.64	0.62	0.46	0.46

Figure 7. Comparing the initial five design points. The first design is selected as the optimal wing configuration.

The Pareto curve in the aeroelastic analysis, shown in Figure 8, of a composite wing illustrates the trade-off relationship between wing skin weight and unit twist factor. The horizontal axis denotes variations in skin weight, while the vertical axis represents changes in the unit twist factor. The curve itself, known as the Pareto front, comprises points representing solutions that are Pareto optimal, meaning any improvement in one objective comes at the expense of the other. Regions where constraints are satisfied, constraints are failed, and the Pareto solutions are distinguished. This visual representation makes informed decisions, with design points on the Pareto curve being selected that align with specific priorities, thereby providing a clear understanding of the trade-offs between conflicting objectives in the optimization process.

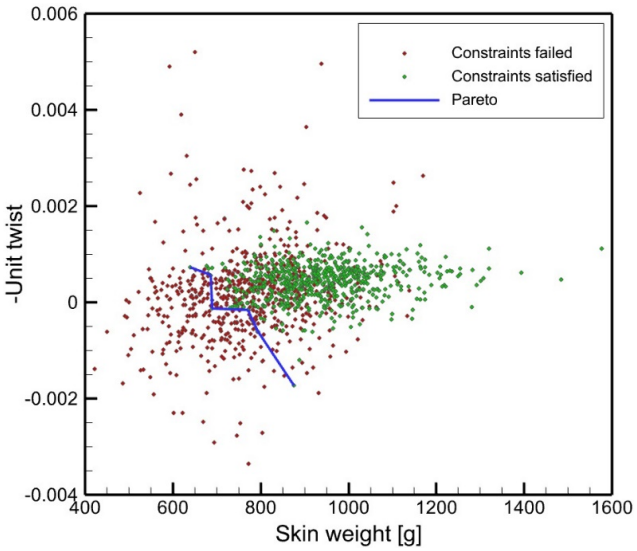

Figure 8. Pareto curve.

In Figure 9, the stacking sequence in the composite wing configuration is given, revealing the arrangement of the upper and lower skins along with the spar. To enhance design adaptability, the upper and lower skins, strategically incorporated as optimization variables, are subdivided into three distinct regions, each characterized by varying lengths, as visually represented in Figure 6. For tapered upper and lower skins, a unique fiber angle is exhibited by each layer and region, highlighting a distinctive feature. The spar, attributed to its primary role in bearing aerodynamic loads, maintains a consistent fiber angle across its entire span. Emphasizing the symmetric layout inherent in the stacking sequence of both the skins and the spar, this symmetry plays a crucial role in ensuring overall structural integrity and balance in the design. These region lengths and their corresponding outcomes are presented in Figure 9.

(a) Upper skin

Sections [mm] / Layer	L_1^U	L_2^U	L_3^U
	130	714	406
1	-30°		
2	20°		
3	50°		
4	30°		
5	20°		
6	45°		
7	-70°		
8	-70°		
9	45°		
10	20°		
11	30°		
12	50°		
13	20°		
14	-30°		

(b) Lower skin

Sections [mm] / Layer	L_1^U	L_2^U	L_3^U
	132	700	418
1	-20°		
2	30°		
3	-70°		
4	30°		
5	80°		
6	-80°		
7	30°		
8	30°		
9	-80°		
10	80°		
11	30°		
12	-70°		
13	30°		
14	-20°		

(c) circular tube spar

Layer	L = 1250 mm
1	0°
2	90°
3	90°
4	0°

Figure 9. Arrangement of the upper and lower wing skins along with the spar in the stacking sequence.

Figure 10 depicts the weight variation of the wing skin during optimization iterations, offering insights into the algorithm's convergence toward the minimum skin weight (not the total wing weight) within the design space. Valid design points adhere to constraints and feasibility within the specified design space, while invalid points violate constraints. Smooth convergence to the minimum weight with valid design points is a

positive outcome in structural optimization. The optimization culminates in a skin weight of 640 g, an assembled wing weight (comprising skins, spars, and ribs) of 785 g, and a final wing weight (including the assembled wing with adhesive and color) of 910 g.

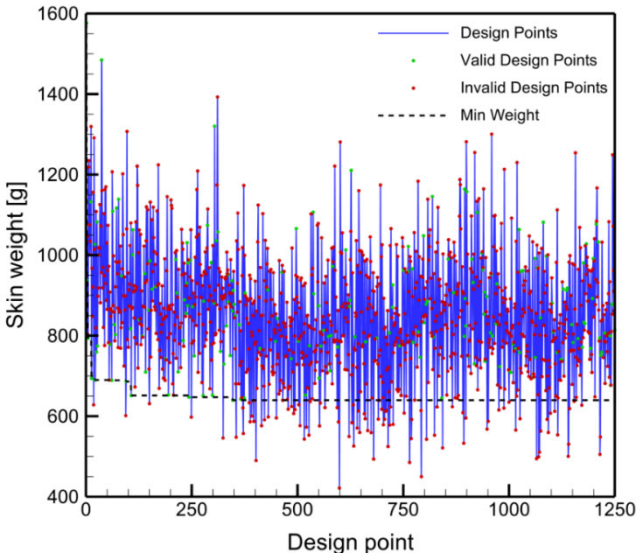

Figure 10. Weight variations during optimization iterations.

6.2.2. Thickness Distribution of the Optimized Wing

In Figure 11, the thickness distribution of both the upper and lower coatings of the composite wing is illustrated, showing a significant layer reduction between regions 1 and 3. The optimization algorithm is specially designed to minimize the number of layers while simultaneously adhering to static strength, failure criteria, and aeroelastic constraints. Its primary objective is to determine the optimal stacking sequence for given configurations. The maximum thickness is observed in the coatings in the first region, while the spar maintains a constant thickness with four layers. As we progress towards the wingtip, a gradual decrease in thickness is observed. Particularly noteworthy is the point of transition between the R_1 and R_2 regions, where the thickness decreases by 34%, making this area more susceptible to failure. Additionally, there is a significant 89% reduction in thickness from the first region to the last region. There is a slight difference in length between the corresponding regions in the the upper and lower skins. The total number of layers in the upper and lower skins for regions R_1, R_2, and R_3 are 14, 8, and 4, respectively.

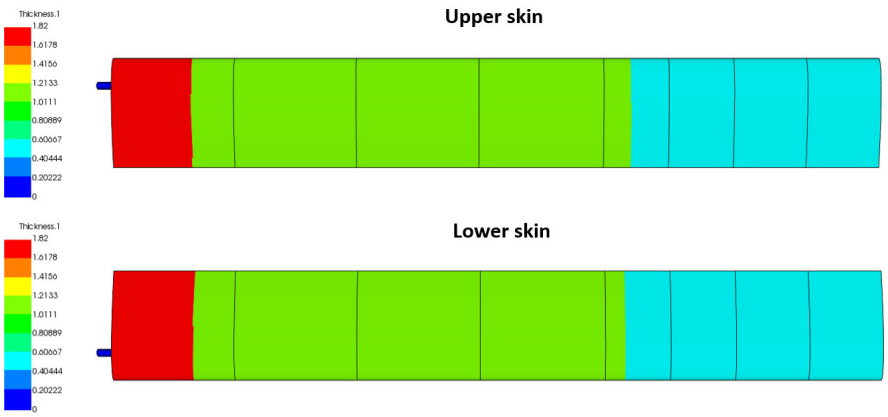

Figure 11. Thickness distribution of upper and lower skins.

6.2.3. Static Flapwise Deformation of the Optimized Wing

Comparing the static deformation of the optimized wing in the flapwise direction, Figure 12 contrasts two methodologies: geometrically linear and nonlinear. At a flight speed of 30 m/s with α = 5° and α = −2.5°, the comparison reveals a significant difference in the wing tip deflection. The nonlinear model, at α = 5°, reveals a 21.1% higher deflection compared to the linear model, exposing the conservative nature of the linear assumptions. Noteworthy is the substantially increased deflection exhibited by the nonlinear model. At higher AOA, these findings stress the significance of accounting for geometric nonlinearity and emphasize the drawbacks of relying only on linear assumptions. Wings experiencing such conditions encounter elevated aerodynamic loads and heightened system nonlinearity due to larger deformations. Emphasizing the imperative need to incorporate geometric nonlinearity for more precise and dependable results, this study addresses misleading outcomes from the linear model.

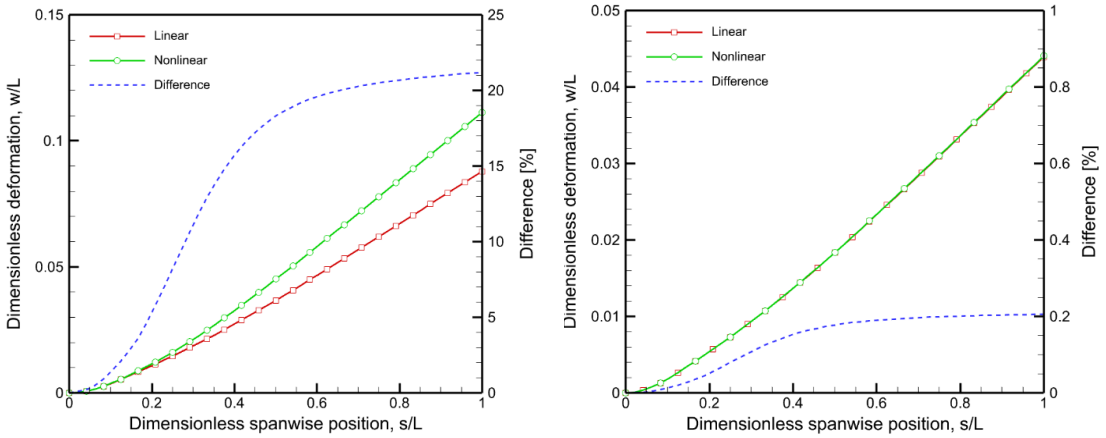

Figure 12. Comparing the vertical deformation of the optimized wing with both geometric linearity and nonlinearity for AOAs (**a**) α = 5° and (**b**) α = −2.5°.

6.2.4. Inverse Reverse Factor (IRF) and Buckling Distribution of the Optimized Wing

The reciprocal of the ratio between applied stress or load and critical stress or load, known as the inverse reverse factor, serves as a key indicator of structural proximity to failure. This factor is crucial for assessing structural safety, with a lower value indicating a larger safety margin, signifying greater distance from failure. Conversely, a higher IRF suggests a smaller safety margin, signaling closer proximity to failure.

Figure 13a,b highlight a significant difference in the inverse reverse factor between geometrically linear and nonlinear solutions. ANSYS ACP is employed for the analysis of composite failure criteria. This contrast emerges when accounting for large deformations in the wing under aerodynamic loads. In the nonlinear solution, vulnerable zones in the upper and lower skins, especially the leading-edge part of the upper skin and transition areas of regions 1 and 2, are prone to structural and composite failure. This susceptibility is notably pronounced when reducing the number of layers from 14 in R_1^U to 8 layers in R_2^U. Nearing their structural integrity limits are specific regions of the composite wing, primarily near the root and spar, which are highlighted as other critical areas due to elevated bending moments. This observation suggests these areas are prone to higher stress levels. In linear analysis, the lower skin shows a higher susceptibility to failure compared to the upper skin, while in the nonlinear solution, the upper skin exhibits a higher susceptibility to failure. Table 5 statistically presents the disparity between linear and nonlinear solutions, revealing a notable 27.53% difference for α = 5°. This discrepancy is attributed to the increased aerodynamic loads on the wing at α = 5° compared to α = −2.5°, leading to more significant deformations and heightened nonlinearity in the system.

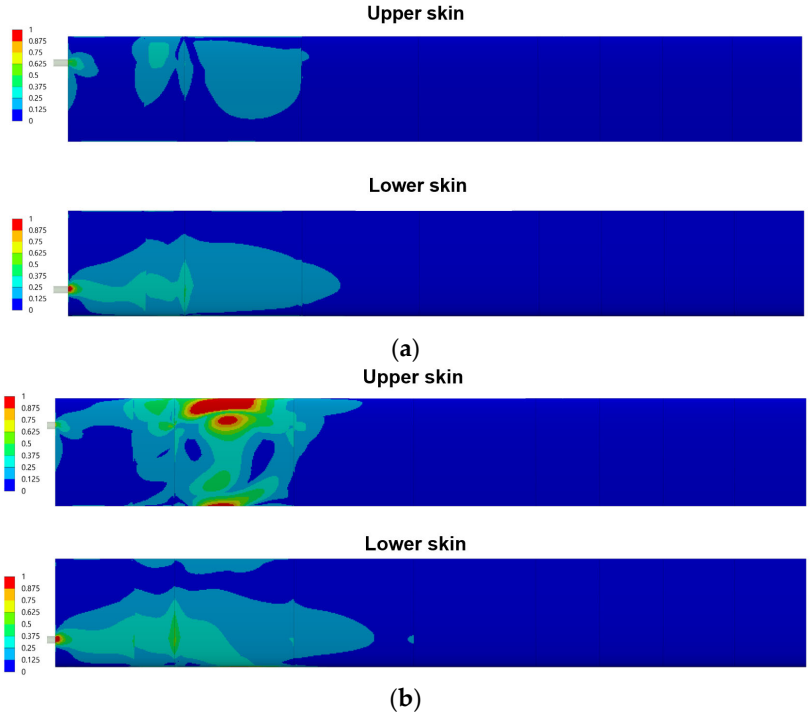

Figure 13. IRF for upper and lower skins for α = 5° (**a**) geometrically linear and (**b**) geometrically nonlinear solutions

Table 5. Comparison of the inverse reverse factor for linear and nonlinear solutions for different AOAs.

Failure Criteria	Linear		Nonlinear	
	α = 5°	α = −2.5°	α = 5°	α = −2.5°
Inverse reverse factor	0.69	0.34	0.88 (+27.53%)	0.33 (−2.93%)

The buckling load multiplier, encompassing global, local, and structural element buckling modes, is the ratio of the critical buckling load to the applied load. The first buckling load multiplier modes are derived under the assumption of geometric nonlinearity for two distinct load case scenarios. Specifically, the buckling load multipliers for angles of attack (AOAs) α = 5° and α = −2.5° at a velocity of U = 30 m/s are found to be 1.11 and 2.53, respectively.

6.2.5. Structural Dynamic, Aeroelastic Instability, and Gust Response

Figure 12 displays the natural frequencies and the corresponding mode shapes of the optimized composite wing. The abbreviations used in Figure 14 include "FB" for flapwise bending, "CB" for chordwise bending, and "T" for torsion. The first three modes are 1st FB, 1st CB, and 2nd FB, while the fourth and fifth modes represent coupling modes of torsion and flapwise bending.

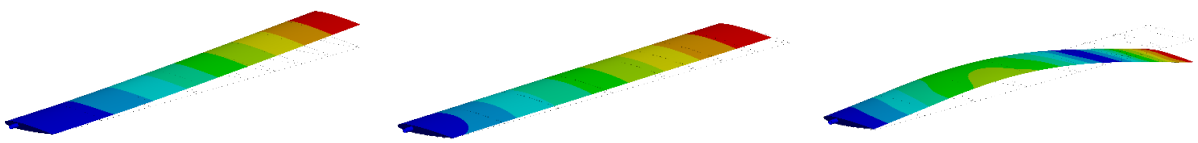

ω_1 = 8.7 Hz (1st FB) ω_2 = 10.86 Hz (1st CB) ω_3 = 51.51 Hz (2nd FB)

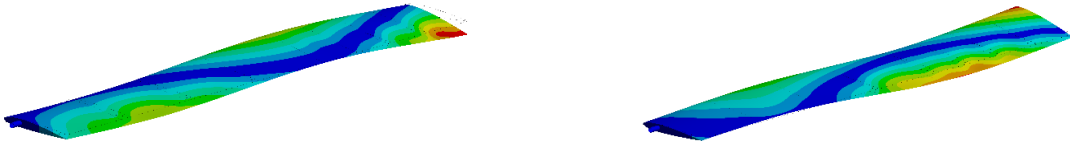

$\omega_4 =$ 127.81 Hz (coupling T & FB) $\omega_5 =$ 139.73 Hz (coupling T & FB)

Figure 14. Natural frequencies and corresponding mode shapes of the clamped wing.

Known as the P-K method, the current flutter analysis technique exploits an unsteady aerodynamic design based on simple harmonic motion for accurate prediction of flutter boundaries. In this method, $k = \frac{b\omega}{U}$ represents the reduced frequency, where $\frac{1}{k}$ denotes the reduced speed. Here, b is the half chord, U is the flutter speed, and ω is the frequency. In this study, the reduced flutter frequency is obtained from the fifth mode's frequency. The resulting reduced flutter speed is shown in both frequency and damping diagrams, as shown in Figure 15a and 15b, respectively. Taking into account geometric nonlinearity, the wing's reduced flutter speed $(\frac{1}{k})$ is determined to be 17.1, surpassing the minimum optimization constraint limit.

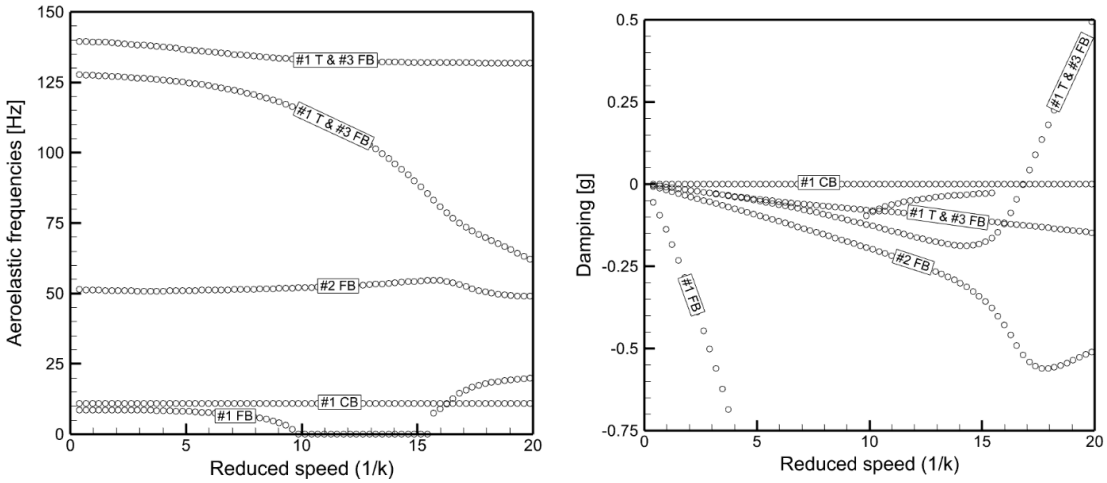

Figure 15. (**a**) Reduced flutter frequency diagram and (**b**) Reduced flutter damping diagram.

Figure 16 illustrates the performance of the optimized composite wing when exposed to the 1-cosine gust model. The primary parameters under investigation for wing gust loading responses are the root bending moment (M_x) and the wing tip deflection (δ_z). The responses are compared for gust velocities WG = 0.1 and frequencies F = 12.5 Hz and 4.5 Hz, shown in Figure 16a and 16b, respectively. These comparisons vividly showcase the performance of the wing model in gusty circumstances at different gust frequencies. The wingtip deflection is characterized by an upward displacement with a positive directional variation. In Figure 16d, the maximum (peak) values of the root bending moment are presented against the variation of gust frequency (F) at WG = 0.1. The gust frequency corresponding to the flight speed of 30 m/s is determined using,

$$\text{Gust Frequency } (F) = \frac{\text{speed of aircraft } (V)}{\text{Gust Length } (25c)} = \frac{30 \text{ m/s}}{4.5 \text{ m}} = 6.66 \text{ Hz} \quad (3)$$

where c is the chord length. In Figure 14d, the highest value of the root bending moment is evident, occurring near 6.66. The first flapwise bending (FB) natural frequency of the wing is approximately 8.7 Hz, significantly distant from the gust frequency. This substantial gap between the natural frequency and gust frequency meets the optimization

constraints, ensuring resilience against gusty conditions. Observing the peak-to-peak distance in the time domain, an approximate gust response time period of around 0.115 s is indicated. If we assume that only the first bending mode is excited, the frequency of the response is expected to be approximately 1/0.115, resulting in 8.69 Hz, which represents the first natural frequency.

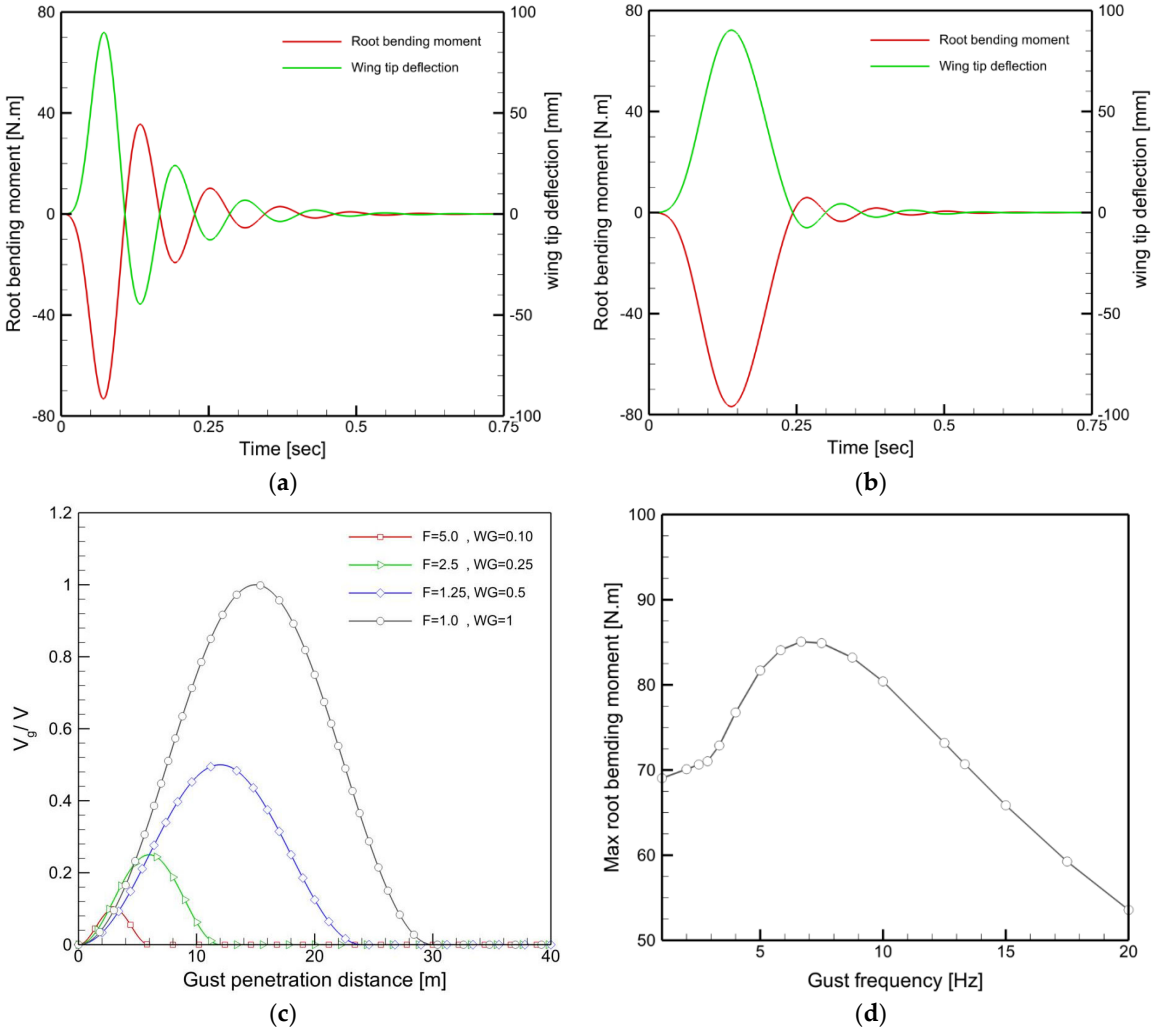

Figure 16. Gust response to 1-cos gust with $WG = 0.1$ and (**a**) gust frequency of 12.5 Hz and (**b**) gust frequency of 4 Hz. (**c**) Gust profile in the vertical direction for various frequencies and magnitudes (**d**) Maximum root bending moment vs gust frequency at $WG = 0.1$.

7. Experimental Results and Discussions

7.1. Manufacturing of the Optimized Composite Wing

To verify the modeling and align with the finite element numerical model for a UAV wing constructed from composite materials, a primary fabrication is conducted, informed by the outcomes derived from the optimization process. To achieve this goal, a dedicated composite workshop has been established within the Department of Aerospace Engineering at Adana ATU. The manufacturing process of the composite wing involves the use of a mold, employing hand layup and vacuum bagging techniques. A collaborative team comprising aerospace engineers and technicians is responsible for carrying out this production.

For our UAV wing project, we chose hand layup and vacuum bagging due to their simplicity, technical efficiency, and cost-effectiveness. Vacuum bagging involves placing fiber material over a mold, saturating it with matrix material, and sealing it in a bag. The vacuum applied during curing ensures consolidation, removes air and voids, and creates a uniform composite structure. This method is cost-effective, allows for higher fiber content, minimizes voids, enhances resin distribution, and results in high-quality composite structures. Figure 17 illustrates the stacking sequence of the top and bottom skins of the composite wing manufactured based on the results of the optimization procedure. Half of the layers are provided due to the symmetry in the skins.

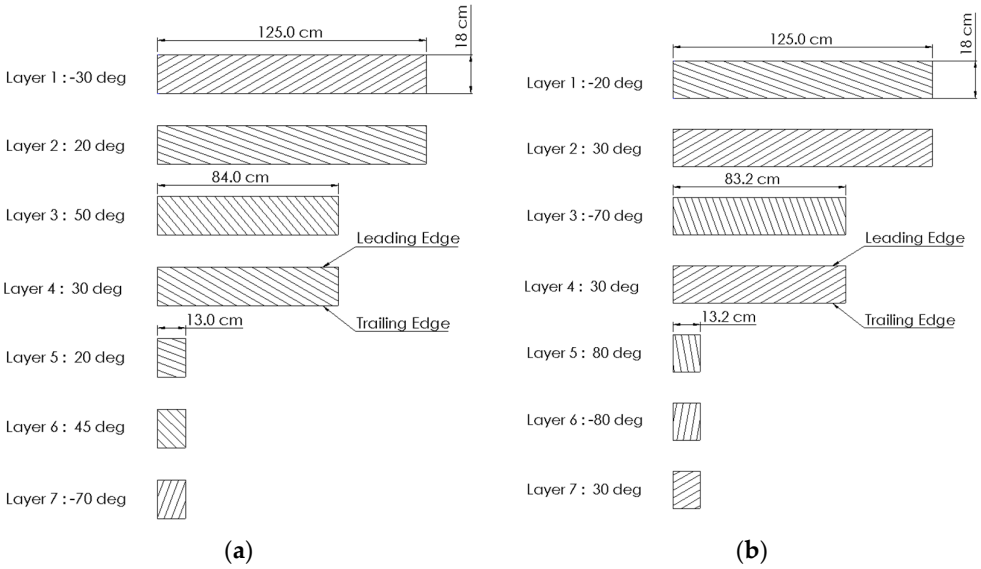

Figure 17. The stacking sequence of the baseline composite wing layout obtained via the optimization process in the (**a**) upper skin and (**b**) lower skin.

Vacuum bagging is a meticulous yet effective technique for manufacturing composite structures, particularly showcased in the creation of a composite wing detailed in Figure 18. Employing unidirectional carbon fiber and a precise pattern paper with a protractor for varied fiber angles, laminas are cut and arranged on an aluminum mold. Mold preparation is critical, involving sealing, release agent application, and thorough drying. A resin mixture is then meticulously applied before layering fabric, adding release film, and breather for resin absorption. Strategic breather placement near vacuum ports prevents issues during curing. The vacuum bagging film, carefully attached with double-sided tape, ensures an airtight seal. Proper sizing and excess film (30–40%) are vital to prevent ruptures. Small slits facilitate vacuum port connections, and a straight hose ensures even distribution. Vigilant inspection and immediate defect resolution maintain a consistent vacuum environment. After resin curing, the composite wing skin is delicately removed, excess material trimmed, and skins cut to specifications. The same process applies to ribs made with sandwiched glass fibers. This method, though labor-intensive, yields high-quality composite structures with attention to detail at each step, showcasing the importance of precision in vacuum bagging for successful composite production.

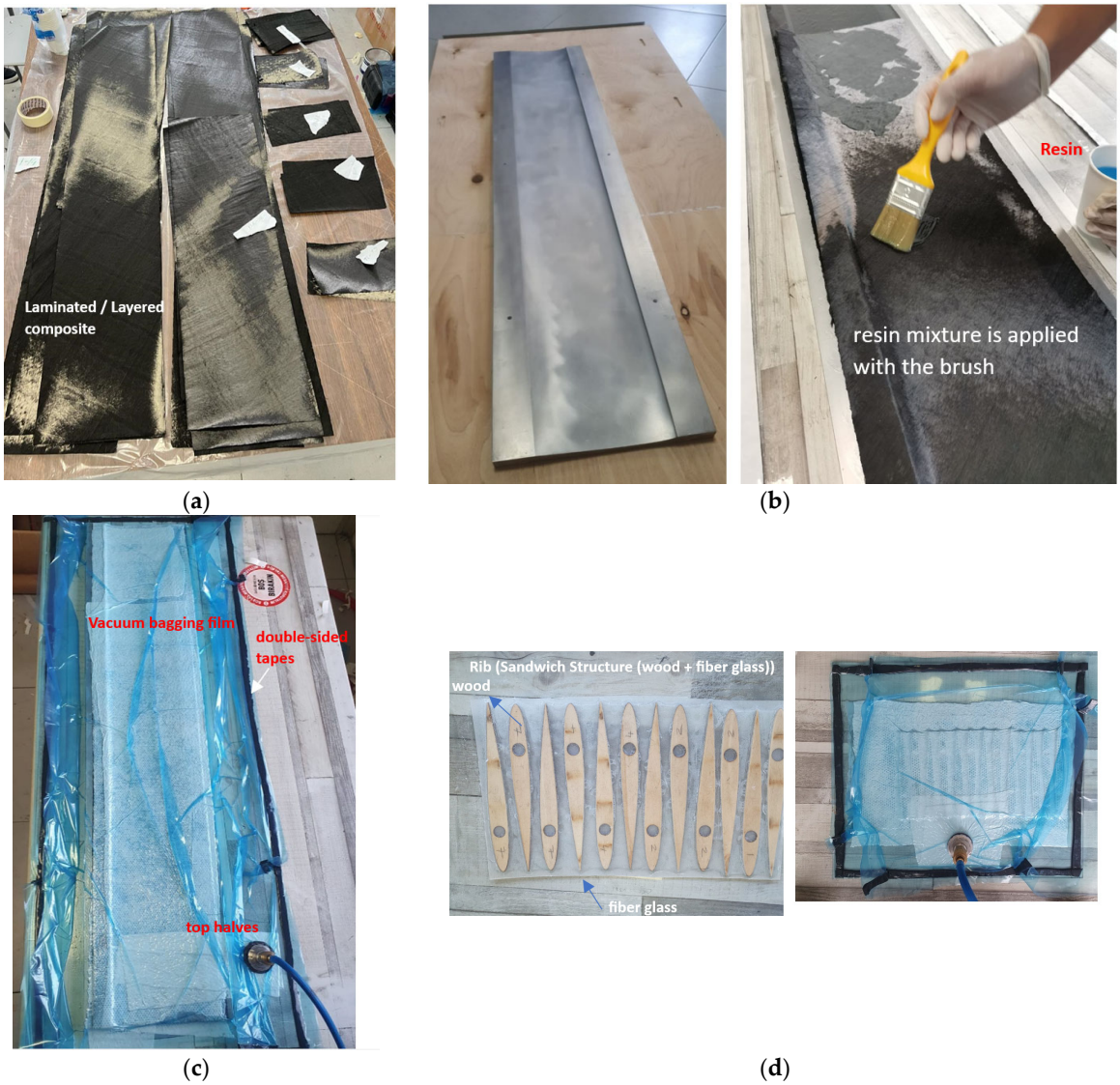

Figure 18. Vacuum bagging process. (**a**) Extraction of the unidirectional fiber at various angles, a pattern paper with a protractor is employed. (**b**) After preparing the surface, the first fabric layer is placed over the pre-wetted mold, and a resin mixture is evenly applied with a brush to saturate it. (**c**) The vacuum bagging film is carefully attached. (**d**) The vacuum bagging procedure is employed for the ribs produced using sandwiched glass fibers.

7.2. Assembling the Manufactured Parts

Following the fabrication of the upper and lower skins, spar, and ribs for the composite wing, the assembly process involves intricately placing the ribs and spar within the lower skin, creating a foundational structure as shown in Figure 19a. With precision, the upper skin is then carefully placed over this assembly. To ensure structural cohesion and integrity, adhesive is applied methodically, forming a robust bond between the upper and lower skins, spar, and ribs, as seen in Figure 19a. An essential aspect of this process is the thorough sealing of the leading edge and trailing edge of the wing, executed meticulously from the root to the tip section. This meticulous attention to detail not only enhances the aerodynamic performance but also reinforces the overall structural robustness of the wing. Finally, for a refined and aerodynamically optimized exterior, a thin layer of black color is delicately applied, contributing to both the aesthetic appeal and functional

efficiency of the composite wing. Figure 19b shows various perspectives of the finalized shape of the assembled composite wing.

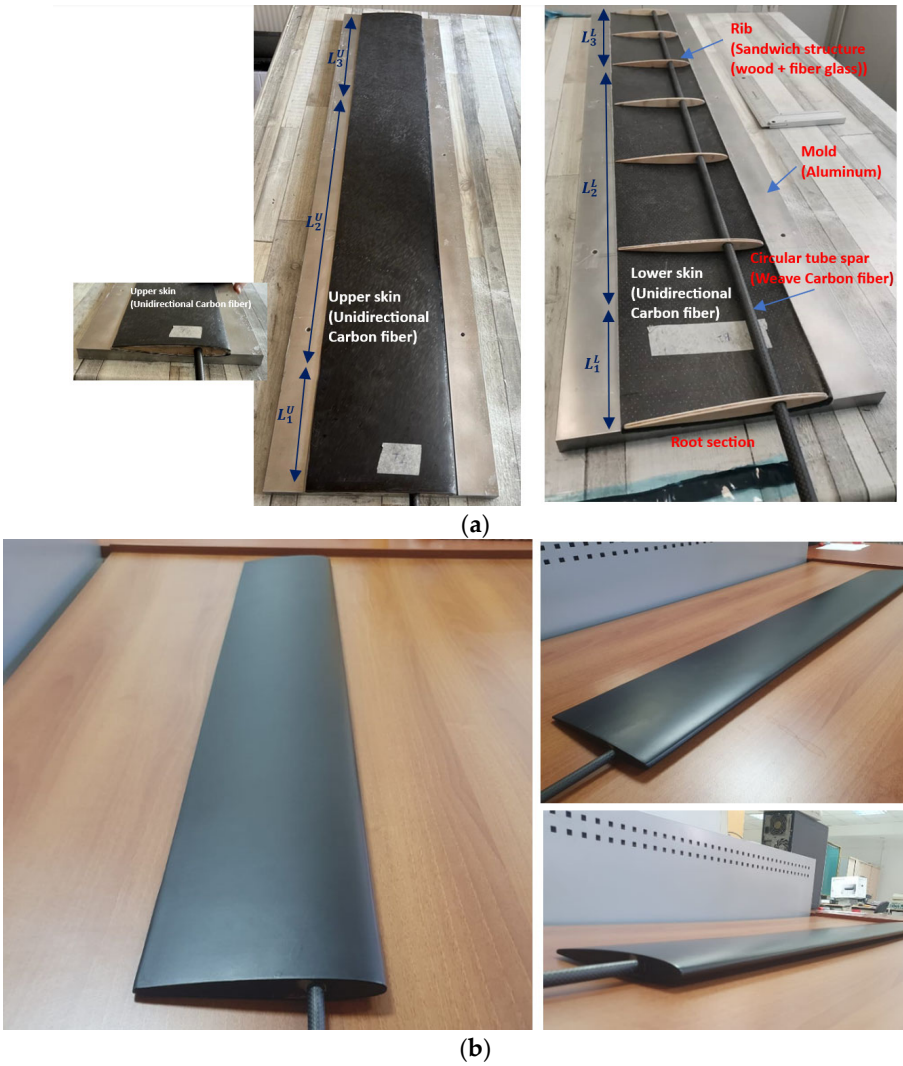

Figure 19. (**a**) Composite wing parts assembly and (**b**) Final views of the composite wing.

7.3. Characterization of the Materials Used in the Composite Wing

The composite materials market offers diverse options with unique combinations of fibers and matrix materials, resulting in varied mechanical properties. Factors such as stacking sequence and environmental conditions further contribute to material variations. Manufacturing processes significantly impact properties, and imperfections can compromise structural strength. Mathematical formulas, for example, the rule of mixtures, based on data from manufacturers, approximate mechanical properties. However, conducting coupon tests is advised due to composites' sensitivity. The composite wing, constructed with unidirectional carbon fibers and a thermosetting epoxy resin using hand layup and vacuum bagging, undergoes tensile testing following ASTM standards. Ultimate strength, stress-strain behavior, and fiber volume fraction (60.2%) are evaluated. Test specimens replicate the conditions visualized in Figure 20. The UD carbon fiber specimen, averaging 4 layers, has a width of 9.2 mm and a thickness of 0.44 mm.

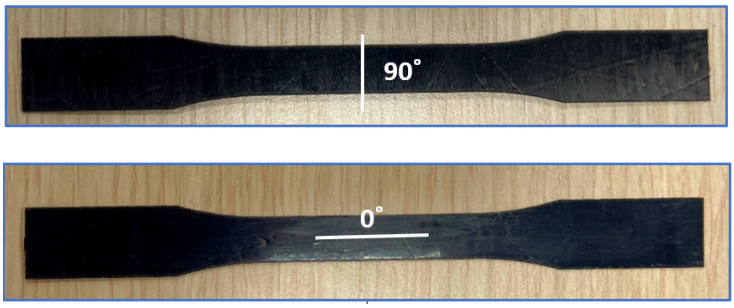

Figure 20. Samples of specimens at 0 and 90-degree orientations.

The Shimadzu Universal Testing Machine, with a 10 kN capacity, conducted tensile, compression, and bending tests on material specimens in this study. Its electric motor-driven unit, operated through built-in keys or 'Trapezium' X software on a PC, facilitated standardized tests and comprehensive documentation, including stress-strain diagrams. Figure 21 shows the testing machine, composite specimen, and software. Experiments took place in the Mechanical Engineering laboratory at Adana Science and Technology University.

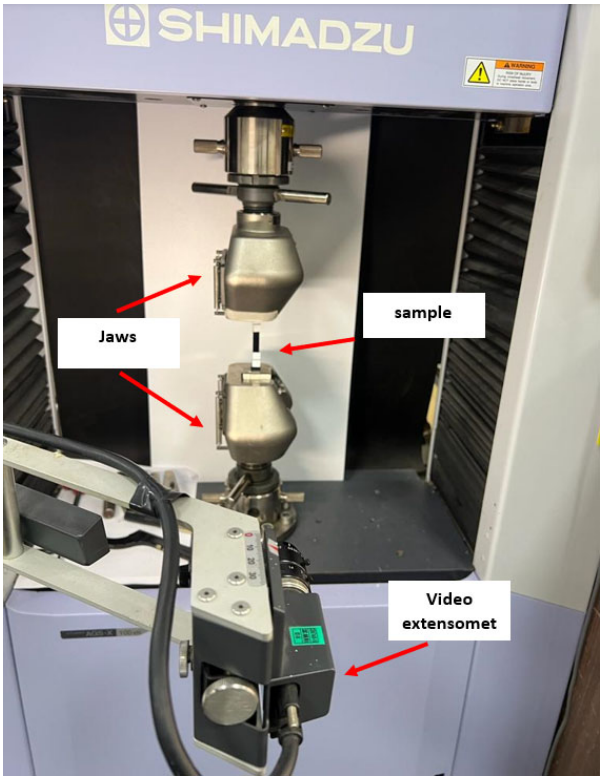

Figure 21. Shimadzu Universal Testing Machines and 'Trapezium X' software.

Specimens, prepared and measured, are securely clamped in the Shimadzu Universal Testing Machine for controlled testing. Parameters such as dimensions, speed (constant at 2 mm/min), and grip separation are input into the software. The test captures a force-displacement diagram, allowing the software to compute elastic modulus, stress, and percent elongation at failure. Results indicate brittle behavior in the tested composite materials, seen in straight stress-strain curves with abrupt failure. Figure 22 illustrates a typical curve with lateral-type failures. Testing is conducted at ambient room temperature, with results considered reasonable and acceptable.

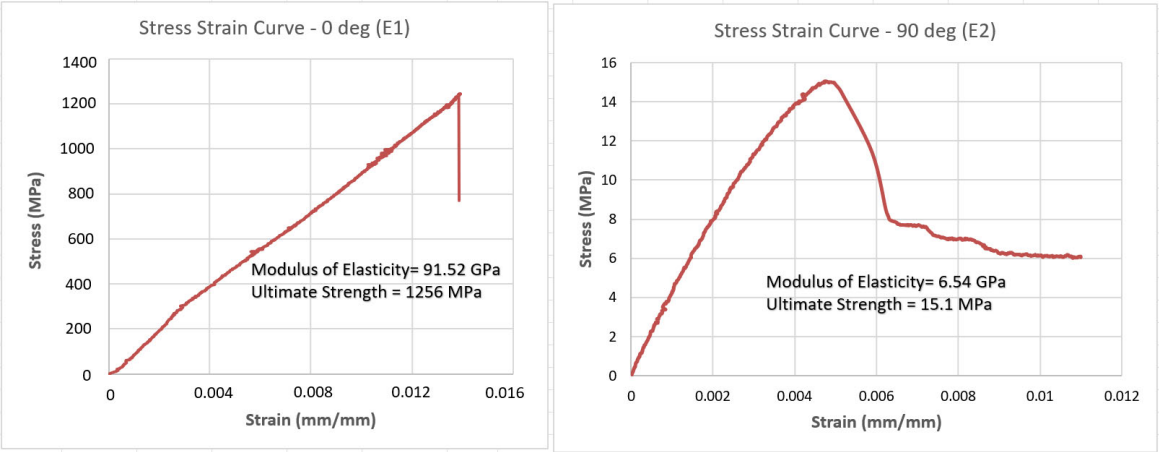

Figure 22. Stress-strain curves for a set of composite specimens.

To evaluate the mechanical characteristics of the laminated composites, test specimens are produced using the hand layup and vacuum bagging techniques, employing a process akin to that discussed in Section 7.1. However, in this instance, a smooth glass mold is utilized, incorporating the same carbon fiber and resin. Through experimental procedures, the mechanical properties of the composite lamina are comprehensively assessed. The outcomes of these experiments, encompassing the resulting properties, are detailed in Table 6. It is important to note that the reported values represent averages derived from a total of three tests conducted using a tensile machine with coupon specimens. To provide insight into the statistical representativity of the data, the average values are accompanied by the standard deviation of these three tests.

Table 6. Characterized properties of the U-D composite.

E_1 (GPa)	E_2 (GPa)	G_{12} (GPa)	ν_{12}	ϱ (kg/m^3)
91.52	6.54	3.6	0.27	1490
XT (MPa)	XC (MPa)	YT (MPa)	YC (MPa)	S (MPa)
1256.0	822.3	15.1	76.0	45.6

7.4. Experimental Modal Tests of the Optimized Composite Wing

The experimental setup in the Department of Aerospace Engineering at the Middle East Technical University used for the experimental modal analysis (i.e., Ground Vibration Tests (GVT)) comprises a test structure (i.e., a composite wing (Figure 23)) having free-free boundary conditions, which eliminates constraint-induced errors in modal analysis and enhances the accuracy by also ensuring that the identified vibration modes are not influenced by artificial constraints. This configuration also improves the correlation between experimental and analytical results, which is a key aspect of modal analysis.

During the modal testing, a Brüel&Kjaer 4524B type Triaxial DeltaTron accelerometer is used to measure the acceleration of the wing located at the tip (i.e., at measurement point 36 in Figure 23), and a Brüel&Kjaer Type 8206 impact hammer (Figure 24) is used to excite the wing to obtain frequency response functions (FRFs) through the Brüel&Kjaer PULSE spectrum analyzer (Figure 24).

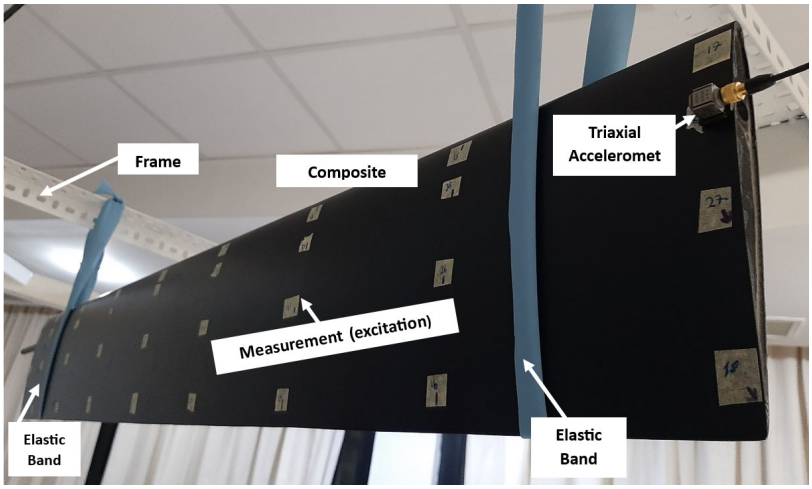

Figure 23. Composite wing structure with free-free boundary condition.

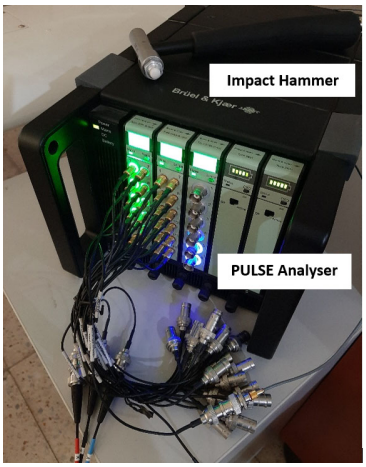

Figure 24. Impact Hammer and PULSE Spectrum Analyser.

In conducting the modal test in a free-free condition, the composite wing is suspended on a frame using two highly elastic bands. The measurement points are chosen at "4 different stations along the chord" (i.e., points located at 0.0 cm (on the leading edge), 5.5 cm (along the spar), 10.5 cm, and 18 cm (on the trailing edge)) and "9 different stations along the span" (i.e., points located at 0.0 cm (at the root), 9.5 cm away from the root, and then 16.5 cm equally spaced locations to the tip) of the composite wing. The experimental grid of the wing, indicating 36 measurement points in total, is shown in Figure 25.

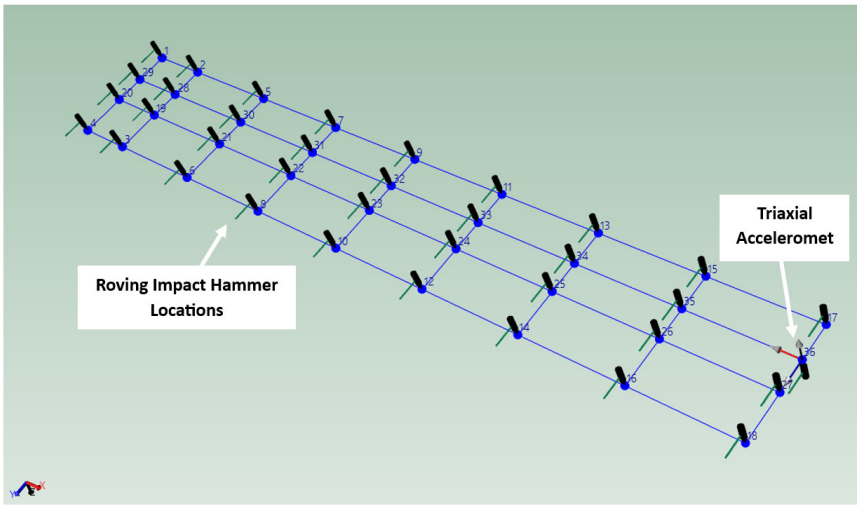

Figure 25. Experimental grid (measurement points) of the wing.

The roving hammer method (with a frequency span of 400 Hz and by zooming into 280 Hz, covering the first four global modes of the wing with 800 FFT lines through linear spectrum averaging over three hits at each measurement point) is performed at 36 different locations, and corresponding frequency response functions are obtained and provided in Figure 26.

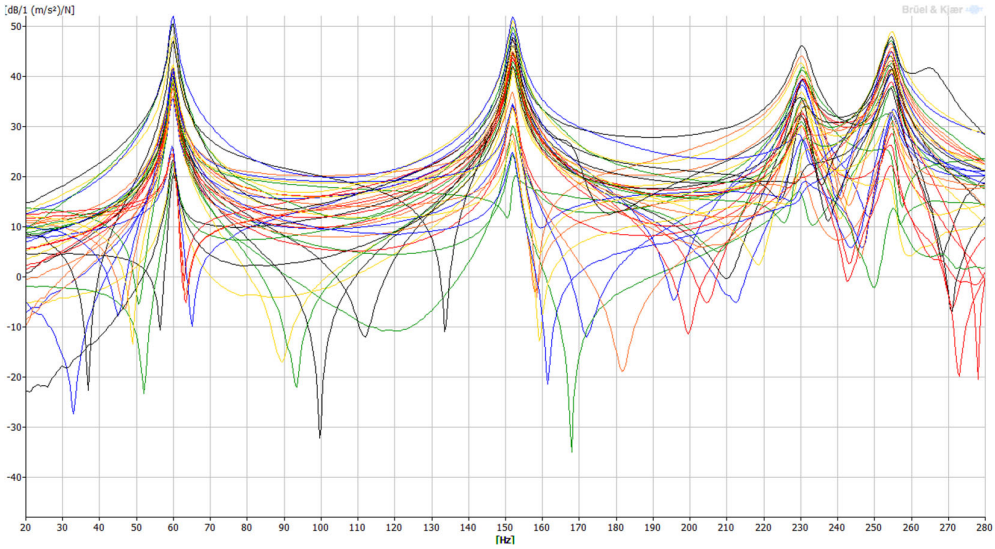

Figure 26. Frequency response functions (accelerance) of the roving hammer measurements.

The stability diagram (Figure 27) is drawn using the Rational Fraction Polynomial-Z method after 40 iterations in order to calculate the resonant frequencies and visually obtain the corresponding mode shapes that are given in Figure 28. The percentage difference between experimentally obtained resonant frequencies and those of numerically calculated ones are also provided in the same figure in parenthesis. The predictions for the first and second out-of-plane bending and torsion are good, with errors of around 1.39%, 1.4%, and 0.72%, respectively. The mode shapes and their order are consistent between NAS[2] and GVT for all modes.

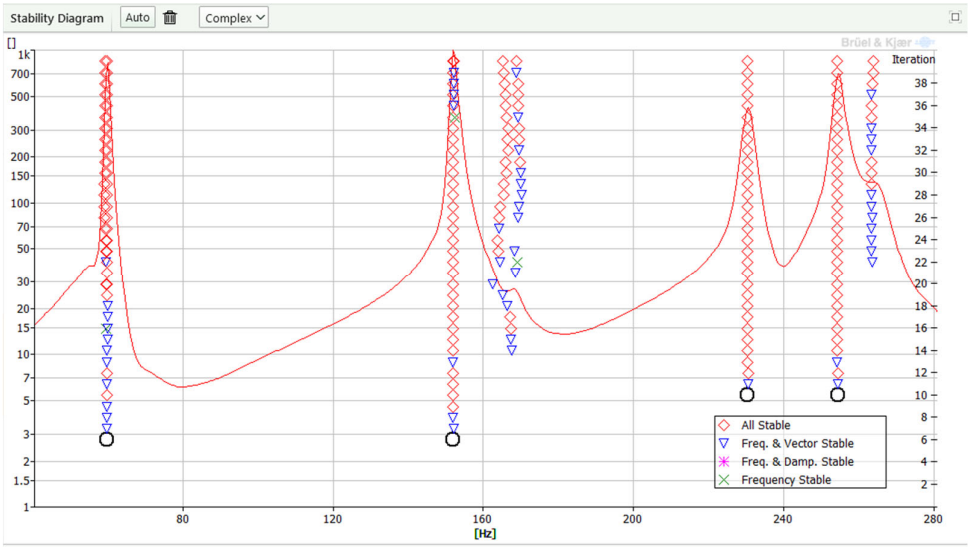

Figure 27. Stability diagram via the Rational Fraction Polynomial-Z method.

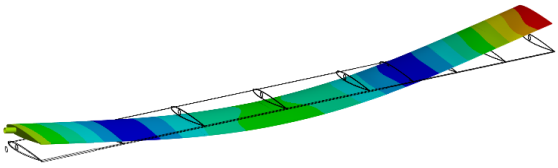

$\omega_1 =$ 59.01 Hz (1st out of plane Bending)
NAS² (1.39%)

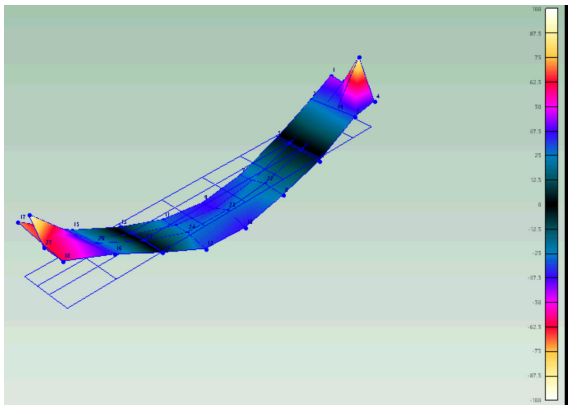

$\omega_1 =$ 59.84 Hz (1st out of plane Bending)
GVT

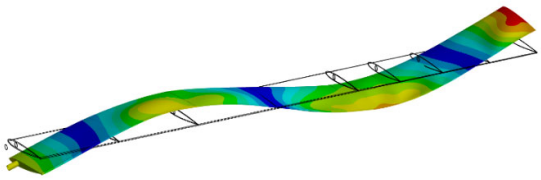

$\omega_2 =$ 149.87 Hz (2nd out of plane Bending)
NAS² (1.40%)

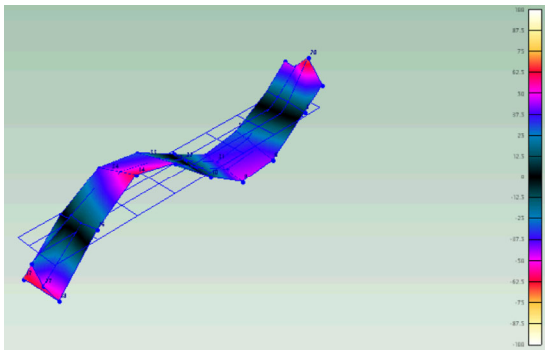

$\omega_2 =$ 151.99 Hz (2nd out of plane Bending)
GVT

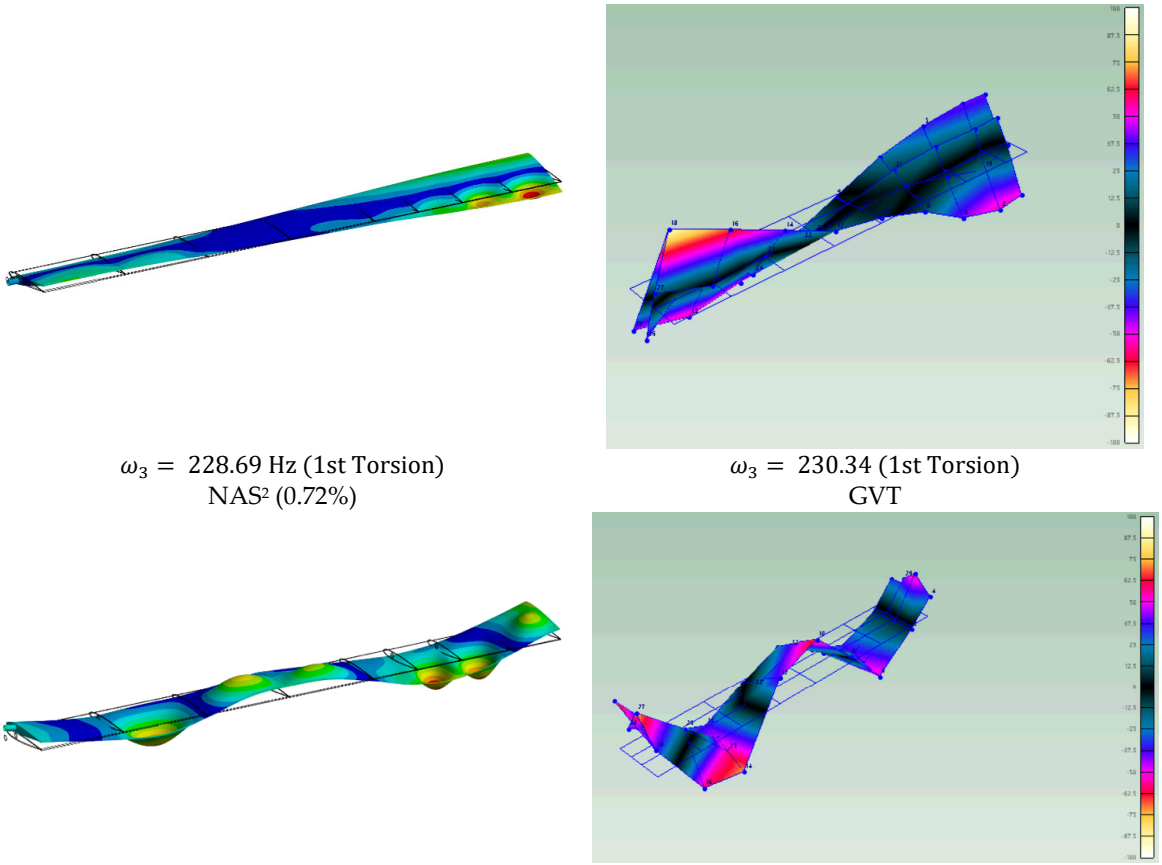

Figure 28. Comparison of natural frequencies and corresponding mode shapes of the wing obtained from the NAS² model and the GVT.

7.5. Experimental Static Deflection of the Optimized Composite Wing

In the experimental procedure for static deflection analysis of an optimized composite wing using a Digital Image Correlation (DIC) system, the setup is established in the Composite Materials Characterization Laboratory at the Middle East Technical University Center for Wind Energy (METUWIND). The experiment employs the GOM ARAMIS 4M DIC system, as shown in Figure 29, featuring two cameras, a base, and a slider for three-dimensional contactless deformation measurement. The composite wing is clamped securely using vice jaws, and weights of 374 g, 748 g and 1723 g in three stages, namely stage 1, stage 2, and stage 3, are applied to simulate different loading conditions at the tip of the wing, as shown in Figure 30a. A stochastic color spray pattern is then applied to a designated measurement field, 18 cm away from the tip, enabling the ARAMIS system to accurately capture and analyze displacements and deformations using digital images. The stochastic paint field is applied 18 cm away from the tip for an area of 14 cm × 11 cm, which encloses the measurement points as shown in Figure 30b. The DIC system is calibrated, and sufficient photo images are recorded in both deformed and undeformed states.

Subsequently, the recorded data is processed using the ARAMIS software version 1.02, comparing and calculating displacements and deformations. Concurrently, finite element analysis in NAS² is conducted, importing the experimental data to validate and complement the results obtained from the DIC system. The procedure ensures a comprehensive analysis of the static deflection behavior of the composite wing under different loads, combining the precision of the ARAMIS DIC system with the numerical simulations of NAS² for a thorough understanding of the structural performance of the composite

wing. Results are meticulously documented, encompassing experimental measurements, load values, and any pertinent observations from the DIC system and NAS[2].

Figure 29. DIC test setup of composite wing.

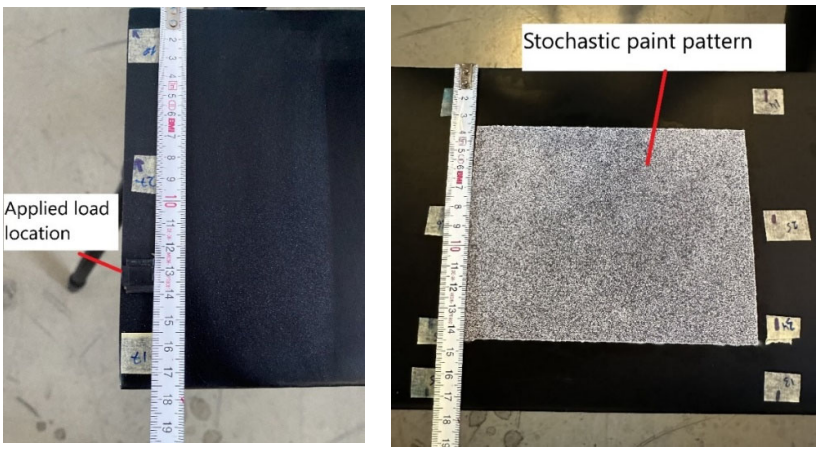

(**a**) (**b**)

Figure 30. (**a**) Location of the load applied and (**b**) dimension of the stochastic pattern.

In Figure 31, an analysis is conducted to compare the static deflection contour, specifically at the designated paint pattern location, for a load of 1723 g. This comparative assessment involves the utilization of both NAS[2] and DIC systems, providing an understanding of the structural response under the specified weight.

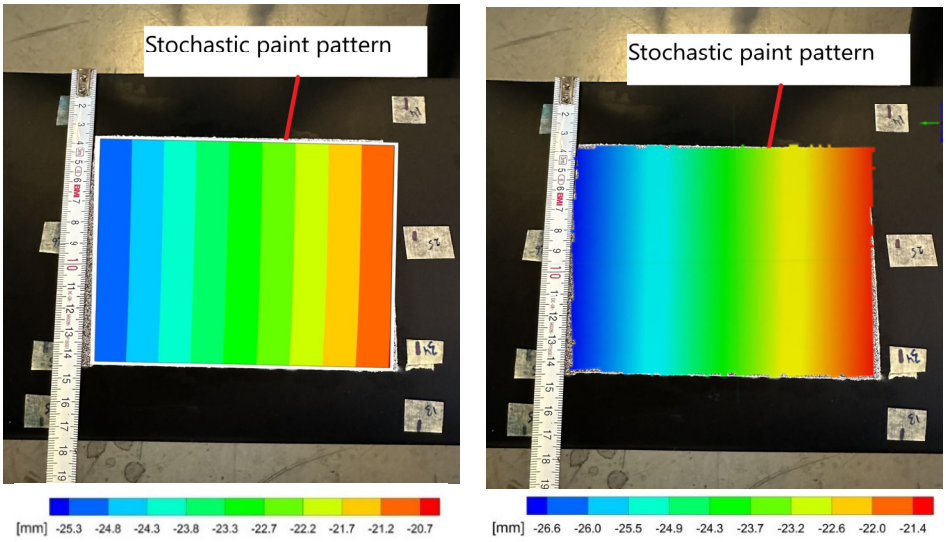

(**a**) NAS² model (**b**) DIC system

Figure 31. Comparing static deflection of the wing obtained from the NAS² model and the DIC system for stage 3 with 1723 g.

Table 7 compares the deflection results obtained by the DIC experimental test and the NAS² numerical solution at the spanwise ends of the painted pattern, which are 93 cm and 106 cm away from the wing root. Three different loadings of 374 g, 748 g, and 1723 g are considered in the static analysis. The NAS² results are in good agreement with the DIC system results.

Table 7. Comparison of DIC and FEM results of the vertical displacement for different sections from the wing root.

Loading	DIC Results	NAS² Results	Diff (%)	DIC Results	NAS² Results	Diff (%)
	δ (mm) @ L = 93 cm from Wing Root			**δ (mm) @ L = 106 cm** from Wing Root		
Stage 1 (374 g)	7.19	7.10	1.25	8.71	8.60	1.26
Stage 2 (748 g)	11.08	10.87	1.89	13.51	13.22	2.15
Stage 3 (1723 g)	21.60	20.70	4.16	26.43	25.30	4.27

8. Conclusions

This research introduces an aeroelastically tailored Multi-objective, Multi-disciplinary Design Optimization (MDO) approach that seamlessly integrates numerical optimization techniques. The aim is to minimize weight and ensure structural integrity, followed by the manufacturing of the optimized wing configuration and performing a Ground Vibration Test to validate and correlate with the numerical model. The proposed numerical methodology, integrated within the fully automated Nonlinear Aeroelastic Simulation Software (NAS²) package, combines FEM code for simulating structural performance, an in-house ROM framework for geometrically nonlinear aeroelastic analyses, and PSO as a population-based stochastic optimization technique. Establishing a robust numerical approach, this integration is designed for the improved aeroelastic and structural performance of composite wings. Through this multidisciplinary approach, we emphasize the pivotal role of tailoring aeroelastic solutions in the advanced design and manufacturing of high aspect ratio composite wings, contributing to the continued evolution of aerospace technology.

- The objective is to comprehend the practical behavior of high aspect ratio wings constructed from composite materials, considering both static and aeroelastic constraints, and assess the efficiency of optimization in enhancing the overall

performance. To achieve this goal, a flexible wing with an aspect ratio of 14 and a span of 1.25 m was specifically designed to be critical in terms of structural, static, and dynamic parameters.

- The optimized wing was constructed using UD TR50S carbon fiber and subjected to a Ground Vibration Test (GVT) for evaluation. The GVT results validated and correlated well with the numerical simulation employed in designing the optimized wing, demonstrating a reasonable accuracy with a maximum difference of less than 6%.
- Across different load cases, the impact of nonlinearity on flutter boundaries may vary. However, it notably impacts the aeroelastic and failure criteria of a composite wing. For the load case with U = 30 m/s and $\alpha = 5°$, differences of 21.1% and 27.5%, respectively, are observed between geometrically linear and nonlinear solutions in terms of static aeroelastic deflection and failure criteria.
- The proposed MMDO method introduces several unique aspects that significantly advance the optimization of composite aircraft structures compared to existing approaches. Firstly, its adoption of a multilayer optimization approach enables the seamless integration of various methods with different levels of accuracy and speed, resulting in a comprehensive system capable of achieving high accuracy and performance. Secondly, the inclusion of unit twist as a parameter in the initial optimization layer serves to expedite subsequent optimization processes, enhancing overall efficiency. Additionally, the method's innovative combination of linear and nonlinear methods ensures a nuanced approach to capturing the complex physics of composite aircraft structure optimization while effectively managing simulation time. This balanced integration ultimately leads to a more comprehensive and efficient optimization process, distinguishing MMDO from existing approaches and promising significant advancements in the field.

Potential areas of future work and recommendations:

- NAS^2 Software Validation: Enhance NAS^2 software reliability through additional validation studies, comparing predictions with wind tunnel experimental data across various angles of attack and Reynolds numbers.
- Industry Impact: MMDO optimization of composite wing designs promises substantial cost savings by reducing material usage and improving structural efficiency. NAS^2's user-friendly interface and robust optimization capabilities make it highly feasible for industry adoption. Integration into existing workflows empowers manufacturers with advanced tools for efficient wing optimization.
- Research Directions: Future research aims to integrate active and passive control surface mechanisms, such as folding wingtip devices, to enhance high aspect ratio wing performance in turbulent conditions. Furthermore, the enhancement of NAS^2 entails the development of an integrated framework for aeroelastic analysis MDO. This involves the integration of Computational Fluid Dynamics (CFD) and Computational Structural Dynamics (CSD) methods to capture superior interaction dynamics, particularly in scenarios with higher Reynolds numbers where viscosity plays a crucial role and in cases of high torsional deformation where dynamic stall may occur.

Author Contributions: Conceptualization, T.F. and M.A.; methodology, T.F., M.A. and M.S.; software, T.F. and M.A.; validation, M.A., M.S. and A.K.; formal analysis, T.F., M.A. and M.S.; investigation, T.F., A.K., H.H.K. and M.I.F.; resources, T.F., A.K. and H.H.K.; data curation, T.F., M.A. and M.S.; writing—original draft preparation, T.F. and M.A.; writing—review and editing, M.S., H.H.K., A.K. and M.I.F.; visualization, T.F., M.A. and M.S.; supervision, T.F., H.H.K., A.K. and M.I.F.; project administration, T.F. and M.A.; funding acquisition, T.F. All authors have read and agreed to the published version of the manuscript.

Funding: This study has been supported by the Scientific and Technological Research Council of Turkey (TÜBİTAK, Grant No. 220N396 and TÜBİTAK 2219 program). T. Farsadi gratefully acknowledges the support of this study.

Data Availability Statement: Available on request.

Conflicts of Interest: The authors declare no conflicts of interest. The funders had no role in the design of the study; in the collection, analyses, or interpretation of the data; in the writing of the manuscript; or in the decision to publish the results.

References

1. Toffol, F.; Ricci, S. Preliminary Aero-Elastic Optimization of a Twin-Aisle Long-Haul Aircraft with Increased Aspect Ratio. *Aerospace* **2023**, *10*, 374.
2. Wunderlich, T.F. Multidisciplinary wing optimization of commercial aircraft with consideration of static aeroelasticity. *CEAS Aeronaut. J.* **2015**, *6*, 407–427.
3. Dillinger, J.K.; Abdalla, M.M.; Meddaikar, Y.M.; Klimmek, T. Static aeroelastic stiffness optimization of a forward swept composite wing with CFD-corrected aero loads. *CEAS Aeronaut. J.* **2019**, *10*, 1015–1032.
4. Zhao, W.; Kapania, R.K. Static aeroelastic optimization of aircraft wing with multiple surfaces. In Proceedings of the 18th AIAA/ISSMO Multidisciplinary Analysis and Optimization Conference, Denver, CO, USA, 5–9 June 2017; p. 4320.
5. Dillinger, J.K.S.; Klimmek, T.; Abdalla, M.M.; Gürdal, Z. Stiffness optimization of composite wings with aeroelastic constraints. *J. Aircr.* **2013**, *50*, 1159–1168.
6. Stanford, B.K.; Jutte, C.V.; Wieseman, C.D. Trim and structural optimization of subsonic transport wings using nonconventional aeroelastic tailoring. *AIAA J.* **2016**, *54*, 293–309.
7. Jutte, C.; Stanford, B.K. *Aeroelastic Tailoring of Transport Aircraft Wings: State-of-the-Art and Potential Enabling Technologies*; (No. NASA/TM-2014-218252); NTRS—NASA Technical Reports Server: Fort Worth, TX, USA, 2014.
8. Stodieck, O.; Cooper, J.E.; Weaver, P.M.; Kealy, P. Improved aeroelastic tailoring using tow-steered composites. *Compos. Struct.* **2013**, *106*, 703–715.
9. Bordogna, M.T.; Lancelot, P.; Bettebghor, D.; De Breuker, R. Static and dynamic aeroelastic tailoring with composite blending and maneuver load alleviation. *Struct. Multidiscip. Optim.* **2020**, *61*, 2193–2216.
10. Belardo, M.; Marano, A.D.; Beretta, J.; Diodati, G.; Graziano, M.; Capasso, M.; Di Palma, L. Wing structure of the Next-Generation Civil Tiltrotor: From concept to preliminary design. *Aerospace* **2021**, *8*, 102.
11. Rafiee, R.; Farsadi, T.; Tehrani, M.A.; Sharifi, P. Linkage Learning Optimization of Aeroelastic and Structural Behavior of Composite Wings. *Int. J. Aeronaut. Space Sci.* **2023**, *24*, 1187–1198.
12. Wang, Z.; Peeters, D.; De Breuker, R. An aeroelastic optimisation framework for manufacturable variable stiffness composite wings including critical gust loads. *Struct. Multidiscip. Optim.* **2022**, *65*, 290.
13. Zhu, Q.; Zhou, L.; Wen, J.; Liu, T.; Zhang, J.; Tang, H.; Zhang, H. Laminar flow over a rectangular cylinder experiencing torsional flutter: Dynamic response, forces and coherence modes. *Phys. Fluids* **2023**, *35*, 093610.
14. Liu, Z.; Zhou, L.; Tang, H.; Wang, Z.; Zhao, F.; Ji, X.; Zhang, H. Primary instability, sensitivity and active control of flow past two tandem circular cylinders. *Ocean. Eng.* **2024**, *294*, 116863.
15. Wen, J.; Zhou, L.; Zhang, H. Mode interpretation of blade number effects on wake dynamics of small-scale horizontal axis wind turbine. *Energy* **2023**, *263*, 125692.
16. Mitrotta, F.M.A.; Rajpal, D.; Sodja, J.; De Breuker, R. Multi-fidelity design of an aeroelastically tailored composite wing for dynamic wind-tunnel testing. In Proceedings of the AIAA Scitech 2020 Forum, Orlando, FL, USA, 6–9 January 2020; p. 1636.
17. Ma, Y.; Elham, A. Designing high aspect ratio wings: A review of concepts and approaches. *Prog. Aerosp. Sci.* **2024**, *145*, 100983.
18. Farsadi, T.; Asadi, D.; Kurtaran, H. Fundamental frequency optimization of variable stiffness composite skew plates. *Acta Mech.* **2021**, *232*, 555–573.
19. Handojo, V.; Himisch, J.; Bramsiepe, K.; Krüger, W.R.; Tichy, L. Potential Estimation of Load Alleviation and Future Technologies in Reducing Aircraft Structural Mass. *Aerospace* **2022**, *9*, 412.
20. Farsadi, T.; Rahmanian, M.; Kurtaran, H. Nonlinear lay-up optimization of variable stiffness composite skew and taper cylindrical panels in free vibration. *Compos. Struct.* **2021**, *262*, 113629.
21. Wang, Y.; Li, X.; Wu, T.; Yin, H. Multidisciplinary Design and Optimization of Variable Camber Wing with Non-Equal Chord. *Aerospace* **2023**, *10*, 336.
22. Benaouali, A.; Kachel, S. Multidisciplinary design optimization of aircraft wing using commercial software integration. *Aerosp. Sci. Technol.* **2019**, *92*, 766–776.
23. Sinha, K.; Klimmek, T.; Schulze, M.; Handojo, V. Loads analysis and structural optimization of a high aspect ratio, composite wing aircraft. *CEAS Aeronaut. J.* **2021**, *12*, 233–243.
24. Silva, G.H.; do Prado, A.P.; Cabral, P.H.; De Breuker, R.; Dillinger, J.K. Tailoring of a composite regional jet wing using the slice and swap method. *J. Aircr.* **2019**, *56*, 990–1004.
25. Saporito, M.; Da Ronch, A.; Bartoli, N.; Defoort, S. Robust multidisciplinary analysis and optimization for conceptual design of flexible aircraft under dynamic aeroelastic constraints. *Aerosp. Sci. Technol.* **2023**, *138*, 108349.
26. Rajpal, D.; Gillebaart, E.; De Breuker, R. Preliminary aeroelastic design of composite wings subjected to critical gust loads. *Aerosp. Sci. Technol.* **2019**, *85*, 96–112.
27. Kilimtzidis, S.; Kostopoulos, V. Static Aeroelastic Optimization of High-Aspect-Ratio Composite Aircraft Wings via Surrogate Modeling. *Aerospace* **2023**, *10*, 251.

28. Kafkas, A.; Kilimtzidis, S.; Kotzakolios, A.; Kostopoulos, V.; Lampeas, G. Multi-Fidelity Optimization of a Composite Airliner Wing Subject to Structural and Aeroelastic Constraints. *Aerospace* **2021**, *8*, 398.
29. Landsberger, B.J.; Dugundji, J. Experimental aeroelastic behavior of unswept and forward-swept cantilever graphite/epoxy wings. *J. Aircr.* **1985**, *22*, 679–686.
30. Chen, G.S.; Dugundji, J. Experimental aeroelastic behavior of forward-swept graphite/epoxy wings with rigid-body freedom. *J. Aircr.* **1987**, *24*, 454–462.
31. Meddaikar, Y.M.; Dillinger, J.K.; Sodja, J.; Mai, H.; De Breuker, R. Optimization, manufacturing and testing of a composite wing with maximized tip deflection. In Proceedings of the 57th AIAA/ASCE/AHS/ASC Structures, Structural Dynamics, and Materials Conference, San Diego, CA, USA, 4–6 January 2016; p. 0489.
32. Krüger, W.R.; Meddaikar, Y.M.; Dillinger, J.K.; Sodja, J.; De Breuker, R. Application of Aeroelastic Tailoring for Load Alleviation on a Flying Demonstrator Wing. *Aerospace* **2022**, *9*, 535.
33. Meddaikar, M.Y.; Dillinger, J.; Ritter, M.R.; Govers, Y. Optimization testing of aeroelastically-tailored forward swept wings. In Proceedings of the IFASD 2017—International Forum on Aeroelasticity and Structural Dynamics, Como, Italy, 25–28 June 2017.
34. Ritter, M.; Dillinger, J.; Meddaikar, Y.M. Static and dynamic aeroelastic validation of a flexible forward swept composite wing. In Proceedings of the 58th AIAA/ASCE/AHS/ASC Structures, Structural Dynamics, and Materials Conference, Grapevine, TX, USA, 9–13 January 2017; p. 0637.
35. Turgut, T. Manufacturing and Structural Analysis of a Lightweight Sandwich Composite UAV Wing. Master's Thesis, Middle East Technical University, Ankara, Turkey, 2007.
36. Rajpal, D.; Mitrotta, F.M.A.; Socci, C.A.; Sodja, J.; Kassapoglou, C.; De Breuker, R. Design and testing of aeroelastically tailored composite wing under fatigue and gust loading including effect of fatigue on aeroelastic performance. *Compos. Struct.* **2021**, *275*, 114373.
37. Farsadi, T.; Rahmanian, M.; Kayran, A. Geometrically nonlinear aeroelastic behavior of pretwisted composite wings modeled as thin walled beams. *J. Fluids Struct.* **2018**, *83*, 259–292.
38. Farsadi, T.; Rahmanian, M.; Kayran, A. Reduced order nonlinear aeroelasticity of swept composite wings using compressible indicial unsteady aerodynamics. *J. Fluids Struct.* **2020**, *92*, 102812.
39. Tang, D.; Dowell, E.H. Experimental and theoretical study on aeroelastic response of high-aspect-ratio wings. *AIAA J.* **2001**, *39*, 1430–1441.
40. Gray, A.C.; Riso, C.; Jonsson, E.; Martins, J.R.; Cesnik, C.E. High-fidelity Aerostructural Optimization with a Geometrically Nonlinear Flutter Constraint. *AIAA J.* **2023**, *61*, 2430–2443.
41. Chao, A.; Chao, Y.; Changchuan, X.; Lan, Y.A.N.G. Flutter and gust response analysis of a wing model including geometric nonlinearities based on a modified structural ROM. *Chin. J. Aeronaut.* **2020**, *33*, 48–63.
42. Riso, C.; Cesnik, C.E.S. Geometrically Nonlinear Effects in Wing Aeroelastic Dynamics at Large Deflections. *J. Fluids Struct.* **2023**, *120*, 103897.
43. Jonsson, E.; Riso, C.; Lupp, C.A.; Cesnik, C.E.; Martins, J.R.; Epureanu, B.I. Flutter and post-flutter constraints in aircraft design optimization. *Prog. Aerosp. Sci.* **2019**, *109*, 100537.
44. Hodges, D.H. Geometrically exact equations for beams. *Encycl. Contin. Mech.* **2020**, 1042–1049.
45. Yu, W.; Hodges, D.H.; Ho, J.C. Variational asymptotic beam sectional analysis–an updated version. *Int. J. Eng. Sci.* **2012**, *59*, 40–64.
46. Farsadi, T. Aeroelastic Analysis of Composite Wings and Wind Turbine Blades Including Geometrical Nonlinearity and Compressibility. Ph.D. Thesis, Middle East Technical University, Ankara, Turkiye, 2018.
47. Librescu, L.; Song, O. *Thin-Walled Composite Beams: Theory and Application*; Springer Science Business Media: Berlin/Heidelberg, Germany, 2005; Volume 131.
48. Sina, S.A.; Farsadi, T.; Haddadpour, H. Aeroelastic stability and response of composite swept wings in subsonic flow using indicial aerodynamics. *J. Vib. Acoust.* **2013**, *135*, 051019.
49. Permoon, M.R.; Farsadi, T. Free vibration of three-layer sandwich plate with viscoelastic core modelled with fractional theory. *Mech. Res. Commun.* **2021**, *116*, 103766.
50. Katz, J.; Plotkin, A. *Low-Speed Aerodynamics*; Cambridge University Press: Cambridge, UK, 2001; Volume 13.
51. Farsadi, T.; Rahmanian, M.; Kurtaran, H. Nonlinear analysis of functionally graded skewed and tapered wing-like plates including porosities: A bifurcation study. *Thin-Walled Struct.* **2021**, *160*, 107341.
52. Rodden, W.P.; Johnson, E.H. *MSC/NASTRAN Aeroelastic Analysis: User's Guide*, Version 68; MacNeal-Schwendler Corporation: Santa ANA, CA, USA, 1994.
53. ZONA Technology, Inc. (ZONA) Available online: https://www.zonatech.com/zaero.html (accessed on 10 January 2023).
54. Balatti, D.; Haddad Khodaparast, H.; Friswell, M.I.; Manolesos, M. Improving Wind Tunnel "1-cos" Gust Profiles. *J. Aircr.* **2022**, *59*, 1514–1528.
55. Kayran, A. Küssner's Function in the Sharp Edged Gust Problem-A Correction. *J. Aircr.* **2006**, *43*, 1596–1599.
56. Asadi, D.; Farsadi, T.; Kayran, A. Flutter optimization of a wing–engine system with passive and active control approaches. *AIAA J.* **2021**, *59*, 1422–1440.
57. Marini, F.; Walczak, B. Particle swarm optimization (PSO). A tutorial. *Chemom. Intell. Lab. Syst.* **2015**, *149*, 153–165.
58. Groenwold, A.A.; Haftka, R.T. Optimization with non-homogeneous failure criteria like Tsai–Wu for composite laminates. *Struct. Multidiscip. Optim.* **2006**, *32*, 183–190.

59. Balatti, D.; Khodaparast, H.H.; Friswell, M.I.; Manolesos, M.; Castrichini, A. Experimental and numerical investigation of an aircraft wing with hinged wingtip for gust load alleviation. *J. Fluids Struct.* **2023**, *119*, 103892.
60. Murua, J.; Palacios, R.; Graham, J.M.R. Assessment of wake-tail interference effects on the dynamics of flexible aircraft. *AIAA J.* **2012**, *50*, 1575–1585.
61. Wang, Z.; Chen, P.C.; Liu, D.D.; Mook, D.T.; Patil, M.J. Time domain nonlinear aeroelastic analysis for HALE wings. In Proceedings of the 47th AIAA/ASME/ASCE/AHS/ASC Structures, Structural Dynamics, and Materials Conference 14th AIAA/ASME/AHS Adaptive Structures Conference 7th, Newport, RI, USA, 1–4 May 2006; p. 1640.
62. Riso, C.; Cesnik, C.E.S. Available online: https://github.com/UM-A2SRL/AePW3-LDWG/tree/main/04_2023_JFS_Riso_Cesnik (accessed on 10 January 2023).